Unione Europea

Ministero dell'Istruzione, dell'Università e della Ricerca

Università degli Studi di Salerno

DIPARTIMENTO DI INGEGNERIA MECCANICA

Dottorato di Ricerca in Ingegneria Meccanica
X Ciclo N.S. (2008-2011)

"Energetic Performances of Regenerators in an Active Magnetic Refrigerator"

Ing. Armando Tura

Armando Tura

Tutor:
Prof. Ciro Aprea

Coordinatore:
Prof. Vincenzo Sergi

Academic Year 2012

Summary

A technology that has the potential to create more efficient and compact refrigeration devices is an Active Magnetic Regenerative Refrigerator (AMRR). An AMRR can operate over a broad range of temperatures, as long as the appropriate refrigerant is implemented. Thus this flexible technology can be used for small, efficient, and simple room temperature refrigerators, as well as efficient gas liquefaction plants (AMRLs). Active Magnetic Regenerator Refrigeration exploits the magnetocaloric effect displayed by magnetic materials whereby a reversible temperature change is induced when the material is exposed to a magnetic field. By using the magnetic materials in a regenerator as the heat storage medium and as the means of work input, one creates an Active Magnetic Regenerator (AMR).

Active Magnetic Regenerator refrigeration systems still rely on correlations between fluid and matrix material to determine the heat transfer coefficient. Typical configurations operate in low Reynolds number and high Prandtl number ranges. For the oscillating fluid flow through these regenerators correlations are used based on single blow experiments. There are large discrepancies for low Reynolds numbers and high Prandtl numbers between the commonly used correlations, even for typically used packed beds, such as packed stainless steel spheres with uniform diameter of 1 mm. Therefore, this thesis addresses the determination of the heat transfer coefficients for oscillating fluid flow with a new approach which combines an analytical model with experimental data. In this work findings for a passive regenerator test apparatus (PRTA) are determined based on thermal and hydraulic effects. Experiments are performed for different operational parameters in respect of the low Reynolds number range, for varying fluid flow frequencies, mass flow rates and heat loads. The generated experimental data are the input for the analytical model for the heat transfer coefficient determination. The results are compared to a commonly used correlation for regenerators like Wakao and Engelbrechts correlations.

Acknowledgements

I would like to thank my advisor, Prof. Ciro Aprea, for his support, warmth and understanding; he really made this experience unique. A person who had a special place during my work has been Dr. Angelo Maiorino. His dedication and energy are limitless. I would also like to thank Prof. Vincenzo Sergi for making his equipment and graduate students available for the development of components critical for this research work. Finally I would like to thank everyone in the department who provided valuable assistance and by sharing their own time and expertise.

TABLE OF CONTENTS

List of Figures

Nomenclature

Acronyms

AMR(R)	Active Magnetic Regenerator (Refrigerator)
MCE	Magnetocaloric Effect (adiabatic temperature change)
MR	Magnetic Refrigerator
RTD	Resistive Temperature Device
NTU	Number of Heat Transfer Units

Symbols

A	Cross sectional area/ Surface area
B	Magnetic flux density
C	Heat capacity
D	Diameter
E	Energy
H	Magnetic field intensity
h	Heat transfer coefficient
I	Current
k	Thermal conductivity
L	Inductance/ Length
M	Magnetization
m	Mass/ Mass magnetization
N	Number of atoms
p	Pressure
Q	Energy flux/ heat transfer
r	Radius
Re	Reynold's number/real part
S,s	Entropy, entropy per unit mass/ Entropy generation/ Stroke/
T	Temperature
t	Time
W	Work

Greek

Φ	Utilization
ϵ	Porosity
β	Balance/ Isothermal compressibility/ interfacial area

γ	Thermal conductivity
φ	Fluid thermal capacity
μ	Viscosity/ magnetic permeability
ρ	Density
τ	Period

Subscripts

ref	Reference value
$Curie$	Curie point
C	Cold
H	Hot
x	Location
low	Low
$high$	High
B	Constant field/ Blow
ad	Adiabatic
b	Bed
f	Fluid
P	Pressure/ particle
s	Solid
g	Generation
min	Minimum
max	Maximum
M	Magnetic
rev	Reversible
irr	Irreversible
d	Demagnetizing/ Displacer
o	Outer
I	Inner

Chapter 1

Introduction

1.1 Motivation

Refrigeration is a pervasive technology that has been instrumental in transforming industrial societies throughout the world. Modern refrigeration equipment is reliable, inexpensive, and mature. It is not unrealistic to say there are few design variables that have not been thoroughly studied and optimized in near-room temperature devices. However, one of the difficulties with conventional vapour-compression refrigeration cycles is that most of the better refrigerants are ozone depleting substances consisting of chlorinated fluorocarbons (H/CFCs, HFC), which can also be powerful greenhouse gases. In addition the CFC and HCFC are already banned in some countries. In contrast, magnetic refrigeration (MR) makes use of a magnetic solid as the refrigerant. As the refrigeration temperature decreases, magnetic refrigeration has the potential to offer significantly higher efficiencies than conventional gas cycles in more compact devices. Research into magnetic refrigeration is currently being pursued using low magnetic fields near room temperature in hopes of enabling commercial devices using permanent magnets as the field source. Another avenue of research is low-temperature applications. These devices could be used for cryogenic refrigeration and liquefaction of gases such as hydrogen and natural gas. In particular, current methods of hydrogen liquefaction are capital intensive and relatively inefficient. Magnetic refrigeration has the potential to provide compact and highly efficient devices over a broad range of operating temperatures. Opportunities for improved performance exist with further engineering refinements [1].

1.2 Magnetic Refrigeration

Background

Magnetic refrigeration exploits a property of magnetic materials called the magnetocaloric effect (MCE): the temperature of ferromagnetic materials is observed to rise upon application of a magnetic field. When a material is magnetized, its magnetic moments are aligned, leading to a reduction in its magnetic entropy. If this process is done adiabatically and reversibly the total entropy is constant. Thus, a reduction in magnetic entropy is compensated by an increase in lattice entropy resulting in a temperature increase. MCE can be defined as adiabatic temperature change due to magnetization, or, alternatively, isothermal magnetic entropy change. This property is a strong function of magnetic field intensity and temperature, and is maximized at the magnetic material ordering temperature, known as the Curie temperature. Figure 1-1 shows Gadolinium MCE for a 2 T field. Interestingly, some antiferromagnetic materials cool down rather than warming up under magnetization [2].

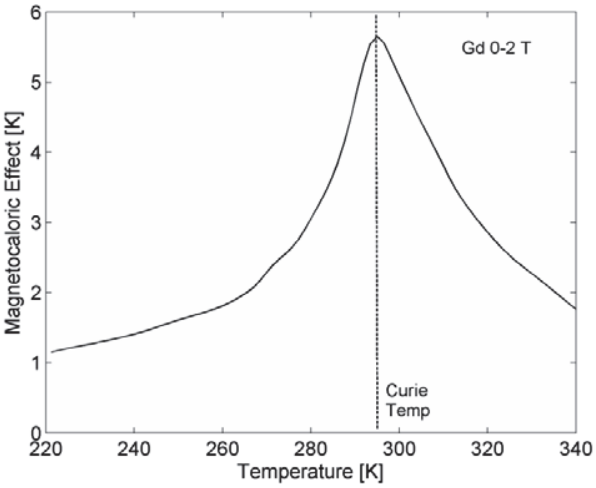

Figure 1-1: Magnetocaloric effect of Gd for a 0-2 T applied field change [1].

Subsequently one can think of using magnetic work to generate thermal cycles, just as compression work is used with gas-cycle refrigeration systems. For instance a Carnot cycle can be obtained by replacing the work of compression with isentropic magnetization.

Magnetic refrigeration was first demonstrated for subkelvin cooling using a “batch cooling” method. The magnetic material, $Gd_2(SO4)_38H_2O$, magnetized at 1.5 K and 0.8 T, was adiabatically demagnetized, thus reducing its temperature to 0.25 K [2]. The batch cooling method is still used for reaching extremely low temperatures, however it cannot be considered a true refrigerator because it does not accomplish a continuous thermal cycle. A cyclic process is necessary for a practical refrigeration device.

Magnetic Refrigeration History

Until the 1970s, magnetic refrigeration remained a means of cooling for low temperatures only. For a material to have a significant magnetocaloric effect, the magnetic entropy change must be large relative to the total entropy of the material. At low temperatures, the lattice and electronic contributions to the entropy are relatively small. Thus, with moderate field changes, it was presumed that magnetic cooling was only effective at low temperatures where the small magnetic entropy changes are relatively large compared to the total entropy [3].

In the 1970s, some exciting progress occurred in magnetic refrigeration. The first breakthrough came with the work of Brown [4][3]. He developed a magnetic refrigerator near room temperature using a reciprocating device based on the Ericsson cycle. Gd was used as refrigerant, a water-alcohol mixture as heat transfer fluid, and a water-cooled 7 T electromagnet. Research on a number of different devices, mostly with rotating and reciprocating geometries, quickly followed.

Then in 1982 a new concept was introduced by Barclay that became known as an Active Magnetic Regenerator (AMR). Unlike previous gas cycles, or magnetic cycles, the AMR concept coupled what had been two separate processes into a single component [3]. Instead of using a separate material as a regenerator to recuperate the heat from the magnetic material, the AMR concept made use of the refrigerant itself as the regenerator. In essence, a temperature gradient is established throughout the AMR and a fluid is used to transfer heat from the cold end to the hot. This subtle but important idea produced a new magnetic cycle distinct from Carnot, Ericsson, Brayton, or Stirling. In the AMR, each section of the regenerator bed undergoes its own cycle; the entire mass of working material no longer experiences a similar cycle at uniform temperature. This concept was given further complexity when the use of multiple magnetic refrigerants in a single AMR was introduced. Early AMR development was focused on the 77 to 20 K range to liquefy hydrogen [3].

During the past decade materials research has been prolific and there have been some interesting new alloys discovered that have the potential to be good magnetic refrigerants for room temperature applications. In particular, a series of ternary alloys in the $Gd_5(Si_xGe_{1-x})_4$ family was found to display high entropy changes due to a first-order phase transition. More recently, a transition metal based compound, $MnFeP_{0.45}As_{0.55}$, has been reported to have a large magnetic entropy change near room temperature again due to a first order phase change. As a result experimental devices have progressed to room temperature applications as time has passed. In 1990 the US Navy David Taylor Research Center in Maryland, conducted a test for room temperature refrigeration using a layered regenerator with a mixed composition of gadolinium and terbium [5]. The magnetic field intensity was varied between 0 and 7 T by ramping the current in the superconducting magnet up and down, in 70 second cycles. Temperature spans up to 50 K were obtained, however the layering concept failed (larger temperature spans were achieved without terbium). While the Cryofuels group at the University of Victoria began working on a rotary AMR to liquefy natural gas, the Astronautics Corporation in cooperation with the Oak Ridge National Laboratory built and tested a medium scale magnetic refrigerator near the liquefaction temperature of nitrogen [6]. The design made use of two 2 kg regenerators reciprocating in a 7 T superconducting magnet. The device produced up to 25 W of cooling, and under no load and a heat rejection temperature of 82 K the cold end of the regenerator reached 44 K. Later, at the Ames Laboratory in Iowa, the Astronautics Corporation built and successfully tested a proof of concept reciprocating room temperature device capable of producing 500 W of cooling power and a coefficient of performance of 6 or more [7]. A helium-immersed superconducting magnet with a field up to 7 T was used. In 1998, researchers at Astronautics Corporation reported a room-temperature device using Gd refrigerant and a water-glycol heat transfer fluid. The cooling power of this device was high, but more significantly, they were able to show refrigeration with an applied field as low as 1.7 Tesla. In collaboration with the Ames Laboratory, this work is now being directed towards the development of a commercial refrigerator near room temperature using permanent magnets. A rotating "magnetic wheel" machine developed at Astronautics was operated for over 1500 h between 2001 and 2007 [1] and it still represents the benchmark for permanent magnet magnetic refrigerators. In 2002 an Active Magnetic Test Apparatus was completed and tested by the Cryofuel Systems group at the University of Victoria. The design and construction was carried out by A. Rowe as part of his doctorate research [3]. The reciprocating device made use of a 2 T superconducting magnet and two AMRs with a mass of up to 135 g each. The refrigerator was designed for flexibility, with the main objective of characterizing a broad range of regenerators, for room temperature and cryogenic applications.

Given the progress in the material development for both permanent magnets and solid refrigerants, prototype design, and interested in more environmentally friendly and efficient refrigeration systems, the International Institute of Refrigeration (IIR) took a step into promoting the development of commercial devices [8]. In 2005 IIR organized the first International Conference on Magnetic Refrigeration at Room Temperature, named Thermag. This biennial event has so far given a substantial momentum to the research and development across the world. Material discovery and system development has flourished and the number of related annually published papers has exponentially increased (Figure 1-2).

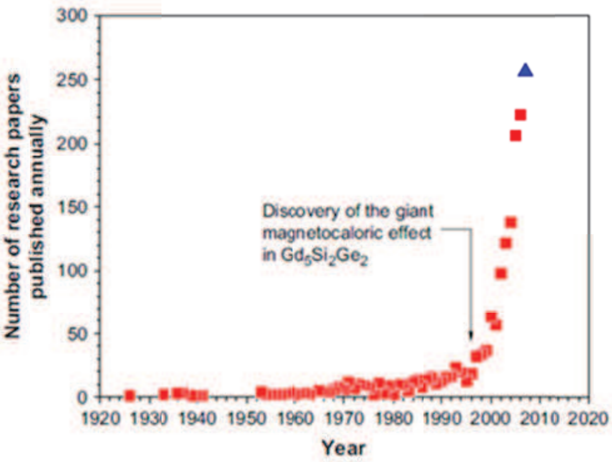

Figure 1-2: Number of publications per year [9].

Among all, the most interesting cooling machines developed during this decade are the Tokyo Institute of Technology's rotating magnet refrigerator (Chubu Electric Power Co.), the Astronautics Corporation's third generation magnetic refrigerator.

Chubu's group targeted a refrigeration machine with a cooling capacity of 500 W and a COP of 3 or greater [10] mainly for air conditioning applications. This was their second generation machine after a proof of concept reciprocating device was previously built and tested [11]. In 2005 a rotary magnetic refrigeration system based on moving permanent magnets and stationary regenerators was developed. The machine originally produced a cooling power of 60 W. Through redesigning the magnets, magnetic yoke, and regenerator flow path the group finally obtained a cooling capacity of 540 W and a COP of 1.8 over a 0.2 K temperature span.

Astronautics Corporation's group developed their third generation refrigerator in 2007. The new design uses a rotating permanent magnet and twelve stationary active regenerators. The choice of a rotating magnet penalizes the design because of the much larger inertial forces, in virtue of simplifying the heat transfer liquid sealing. The machine produced a cooling power up to 220 W with large COP (up to 13) for no temperature span. However the efficiency measurements did not incorporate the mechanical inefficiencies of motors and pumps [12].

Active Magnetic Regenerator

For most contemporary materials, the MCE is modest even near the transition temperature: a material with an adiabatic temperature change larger than 2 K/T is unusual. For example, a sample of gadolinium near room temperature will exhibit a temperature change of approximately 10 K with the application of a 5 T magnetic field. Gadolinium is considered one of the best magnetocaloric materials. It is difficult to produce a useful temperature span based on a Carnot cycle when the effective isentropic temperature change is small. Given the above constraint, one can see the attraction of the active magnetic regenerator (AMR) cycle [1]. A passive regenerator is a highly effective recuperative heat exchanger working in conjunction with a single pulsating fluid stream. If the passive, high heat capacity, material is replaced with an active magnetic material, an AMR is obtained. Acting as a regenerator as well as the means of work input, with the appropriate synchronization of a pulsating fluid and magnetic field, the AMR increases the temperature span many times the adiabatic temperature change as can be seen in Figure 1-3.

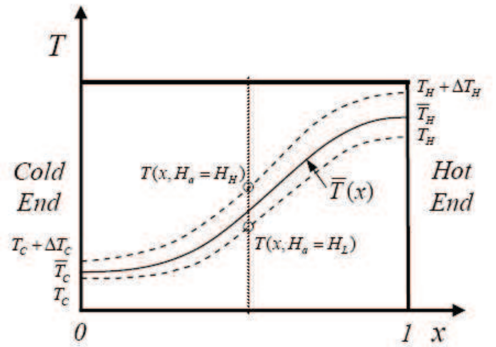

Figure 1-3: The AMR temperature profile at periodic steady state [1].

Like any refrigerator, an AMR operating at periodic steady-state produces a net flow of heat from a cold source to a hot sink. However, a unique feature of an AMR cycle is that at every section of the bed the refrigerant is undergoing its own unique local cycle. Although, the net heat transfer cycle occurs between reservoirs at $\overline{T}_C$ and $\overline{T}_H$, the bulk of the working material does not have to interact with these reservoirs directly. This is conceptually similar to a cascade system of a large number of magnetic refrigerators.

There has been a substantial amount of work regarding the development of materials that should make for good magnetic refrigerants. The assessment of the suitability of these materials has largely rested upon characterization of key thermodynamic properties such as magnetic entropy change, heat capacity, and adiabatic temperature change. It is becoming clear that these properties alone are insufficient in identifying materials that perform well in AMR cycles. Issues such as hysteresis, cost, purity, ease of regenerator manufacture, and relaxation rate all influence the design and performance of AMR coolers. Most importantly, there has been little information reported concerning the dynamic characterization of AMRs and demonstrating actual cooling powers and temperature spans. Systematic investigation of materials in AMR cycles is needed to aid in the development of this technology [13].

1.2.1 Key Parameters

A large number of parameters affect the behavior and the performance of an AMR as illustrated in Table 1-1. These parameters can be categorized as geometric, magnetic, thermofluid, or operational. It is a challenging and lengthy task to experimentally test the system sensitivity for each variable. Furthermore numerical modeling has not been consistently reliable, largely due to the complexity and the non-linearity of the problem as well as uncertainties associated with the material properties.

Table 1-1. Variables in an AMR system.

Geometric	***Magnetic***	***Thermofluid/Operational***
Porosity	Field intensity	Heat transfer fluid
Regenerator shape	AMR material	Utilization, Φ
Regenerator aspect ratio	Field distribution	Frequency
Particle size	Flux shimming	Pressure
		Heat sink temperature
		Cooling
		Phasing

1.2.2 Temperature Profile and Cooling Power

Given an AMR and a set of parameters as defined in Table 1-1, the interest is to pinpoint the performance and to understand the physics underlying the phenomenon. Performance can be quantified by evaluating cooling power, temperature span between hot and cold end, and sensitivity to heat load. In addition, understanding AMR behavior requires knowledge of its thermodynamic properties during operation which can be derived from the AMR temperature distribution. Thus, knowing the temperature distribution allows for the evaluation of cooling power, temperature span, heat load sensitivity, and thermo-magnetic properties of the system.

A practical experimental difficulty is measuring the temperature distribution throughout an AMR in operation. Only a few strategic points along the AMR bed are monitored in the AMRTA. Given the regenerator cylindrical geometry, adiabatic walls, and approximate uniform cross-sectional velocity profile of the fluid, the AMR can be approximated as a 1-D system, simplifying the task of mapping the temperature distribution, which can be condensed to a temperature (1-D) profile. It is expected that a 1-D approximation is most accurate for high aspect ratio regenerators.

1.2.3 Layering

A general scaling relationship giving the ideal MCE as a function of temperature is [3],

$$\Delta T^{ideal}(T) = \big(\Delta T_{ref} + T_{ref)}\big)\left(\frac{T}{T_{ref}}\right)^{\beta} - T \tag{0.1}$$

where ΔT_{ref} is the MCE at a specified reference temperature, T_{ref}, and β is a parameter describing the capacity ratio of the fluid flux for the low and high field flows. For the basic AMR cycle, β is equal to one. In this case, the ideal MCE scales linearly with temperature as,

$$\Delta T^{ideal}(T) = \Delta T^{ideal}(T) = \left(\frac{\Delta T_{ref}}{T_{ref}}\right) \tag{0.2}$$

If the reference temperature is set to be the heat rejection temperature T_H, then ΔT_{ref} is the MCE of the refrigerant at T_H. Assuming the refrigerant is gadolinium and the reference temperature is equal to the Curie point, the ideal MCE can be plotted as shown in Figure 1-4. Clearly, as the temperature moves away from the Curie point of Gd, the real MCE is significantly less than ideal MCE. Thus, the temperature span produce by a real material is much less than can theoretically be supported operating with a heat rejection temperature (T_H) near the Curie temperature.

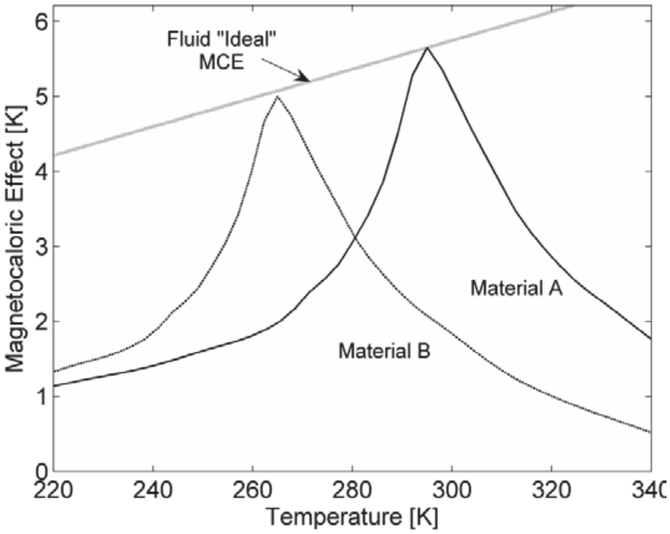

Figure 1-4: The ideal MCE as compared to gadolinium with a 0-2 T field change (Material A), and another material with a Curie temperature near 265 K (Material B).

To compensate for non-ideal material properties, the creation of a single AMR made up of more than one material has been proposed. By layering the AMR with magnetic refrigerants that have increasing Curie temperatures, it may be possible to more closely match the ideal MCE at different locations in the AMR. An example of concept is shown in Figure 1-4.

1.3 Thesis Objective

Current magnetic refrigeration relays on the Active Magnetic Regenerator principle, which performance depends on the MCE of the material, and the thermofluid properties of the regenerator matrix. The research really boils down to improving the MCE and the matrix heat transfer, reducing hydraulic losses, and effectively implementing material layering. It basically branches into three study categories: strictly materials science study (MCE maximization), strictly heat transfer and fluid transport study (regeneration), and a hybrid study that couples the previous two for the layering process.

A vast amount of literature exist that deals with the optimization of passive regenerators used in gas compression devices. Very few, however, deal with heat transfer under oscillating flow conditions using water as a heat transfer fluid as in the present work. Often the packing geometry to be characterized is randomly distributed (such as in particle or crushed particle beds) making direct simulation for extraction of heat transfer data difficult.

This work aims to establishing a clear experimental and theoretical methodology to extract effective hydraulic and thermal transport properties. This objective requires the following activities:

1. Experimentation. This involves an apparatus development, data acquisition handling, and data collection by varying operating parameters as frequency, stroke, heater and cooling load using a microchannel and spheres regenerator.
2. Parameter extraction (Nusselt number and friction factor) of experimental data using simplified macroscopic thermodynamic models.
3. Validation of experimentally found parameters with the available literature.

Chapter 2

Magnetic Refrigeration Theory

2.1 The Magnetocaloric Effect

Magnetic refrigeration exploits a property displayed by certain magnetic materials: the magnetocaloric effect (MCE). In these materials, a significant change in entropy can be effected by the application or removal of a magnetic field, H. For materials with a simple magnetic work mode, the MCE depends only on the absolute temperature of the material, T and the magnetic field change, ΔH (which expresses the difference H_f -H_i) [14]. The MCE can be interpreted as the isothermal entropy change or adiabatic temperature change as it is defined in the following expressions:

$$\Delta S_M(T, \Delta H) = S\left(T, H_f\right) - S(T, H_i) \tag{2.1}$$

$$\Delta T_{ad}(S, \Delta H) = T\left(S, H_f\right) - T(S, H_i) \tag{2.2}$$

Equations (2.1) and (2.2) are graphically illustrated in Figure 2-1(a), where the vertical line is the isothermal entropy change and the horizontal line is the isentropic (adiabatic) temperature change. Both transformations occur between the same $S(T,H)$ curves.

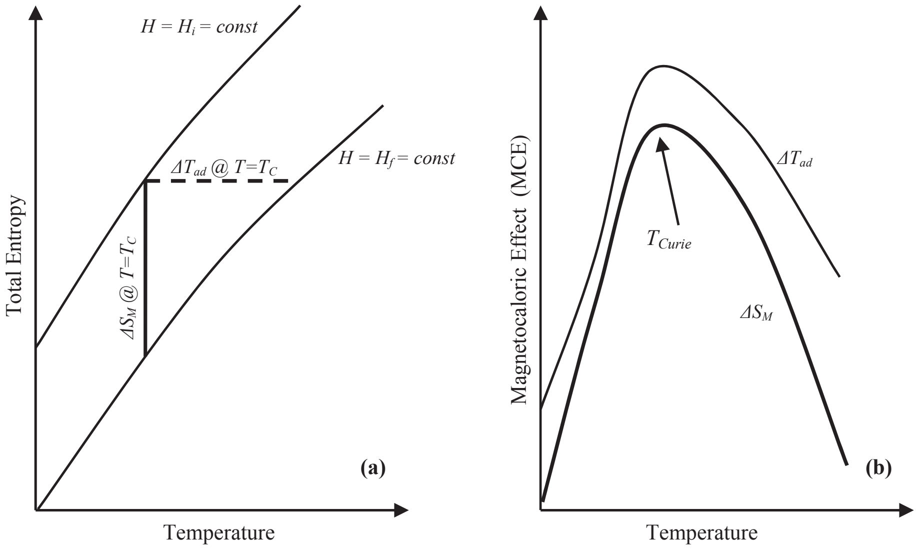

Figure 2-1. Graphical representation of the MCE [14].

Figure 2-1(b) illustrates ΔS_M and ΔT_{ad} for a range of temperatures in the proximity of the Curie temperature, T_{Curie} for $\Delta H = H_f - H_i$. In general, H_i is set to zero. Also a correlation between the MCE and magnetization can be derived. By varying the magnetic field, work is performed and the internal energy of the system changes. Thus, a differential variation in internal energy can be accomplished by a magnetic work interaction given by the product of the applied magnetic field, H, and the variation in magnetization, m [3]:

$$\delta W_m = \mu_0 H dm \tag{2.3}$$

Since for a material that has a simple magnetic work mode, $s = s(T,H)$, a differential change in entropy can be written as:

$$ds = \left(\frac{\partial s}{\partial T}\right)_H dT + \left(\frac{\partial s}{\partial H}\right)_T dH \tag{2.4}$$

where s is the entropy per unit mass. Using the definition of heat capacity, the above can be rewritten as,

$$ds(T,H) = \frac{C_B(T,H)}{T} dT + \left(\frac{\partial s}{\partial H}\right)_T dH \tag{2.5}$$

If an isentropic field change is produced, the temperature change is:

$$dT = -\frac{T}{C_H(T,H)} \left(\frac{\partial s}{\partial H}\right)_T dH \tag{2.6}$$

and using Maxwell's relations for the equivalence of the second derivatives

$$dT = -\frac{T}{C_H(T,H)} \left(\frac{\partial m(T,H)}{\partial T}\right)_H dH \tag{2.7}$$

From this simple explanation, one can deduce that a material with no significant work modes other than magnetic should have a high ratio of magnetic entropy change to total entropy to produce a large adiabatic temperature change. The MCE for a change in magnetic field from 0 to H is related to Equation (2.7) by

$$MCE = -\int_0^H \frac{T}{C_H(T,H)} \left(\frac{\partial m(T,H)}{\partial T}\right)_H dH \tag{2.8}$$

2.2 Materials

Although a broad range of materials that display a significant MCE for a wide spectrum of temperatures are available, research on the development of new materials is still more active than research on AMR cycles. A good refrigerant needs to feature a number of properties to perform satisfactorily in an AMR [4]:

a. An MCE as large as possible, over a broad temperature range allows large cooling power and temperature span, with low sensitivity to heat rejection temperature.

b. Minimal magnetic and thermal hysteresis allows high operating frequency and, consequently, large cooling power.

c. High specific heat improves power density.

d. High thermal conductivity improves regenerator effectiveness.

e. Large electrical resistance minimizes eddy currents.

f. Good mechanical properties simplify manufacturing process.

g. Low material cost is necessary for a commercial viability.

Currently, first order phase transition materials seem impractical for magnetic refrigeration even if they display a very large MCE. This may be due to hysteresis in the phase transformation and narrow MCE curves in the T_{Curie} vicinity. Gadolinium alloys are presently the prototype materials for room temperature magnetic refrigeration because of their good thermo-magnetic properties and since they are best characterized materials [3] in terms of magnetization, heat capacity, and magnetocaloric effect.

2.3 AMR Theory

The system under consideration is shown schematically in Figure 2-2. The envelope of an AMR bed is shown with a dashed line while a section of infinitesimal thickness is drawn with a solid line. The bed is made up of a porous solid material that is the magnetic refrigerant and a fluid within the pores acts as the heat transfer medium. The fluid transfers heat between a cold heat exchanger, the refrigerant, and a hot heat exchanger. The capacity rates of the fluid are shown as $\dot{\varphi}$ (where $\dot{\varphi} = \dot{m}c_p$). Over a complete cycle, heat is absorbed at the cold end and rejected at the hot end. The AMR should be recognized as the combined solid-fluid system [3].

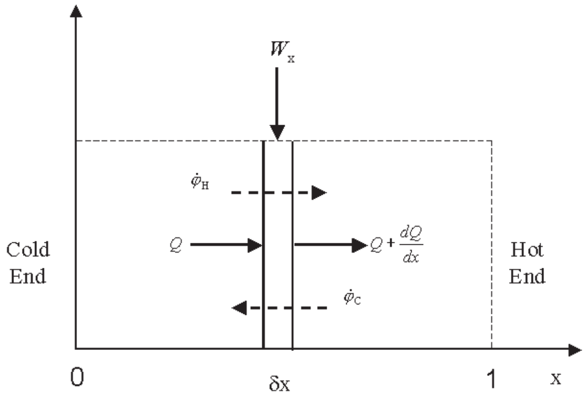

Figure 2-2. A schematic representation of an AMR showing the net work and heat flux at a differential section [3].

Most AMR devices built and tested to date have mimicked a reverse magnetic Brayton cycle in each section of the regenerator bed by using four distinct steps represented in Figure 2-3:

a. The bed is in a demagnetized state. Fluid flows through the regenerator entering the bed at a temperature T_H. As the fluid flows through the bed it exchanges heat with the solid refrigerant and exits the bed at T_C
b. The bed is exposed to a high magnetic field and the temperature of the refrigerant increases due to the magnetocaloric effect by $\Delta T(T)$
c. After absorbing a heat load and increasing its temperature by ΔT_C, the fluid enters the cold end of the regenerator, absorbs heat from the solid and exits the AMR at a temperature $T+\Delta T_H$
d. The AMR is demagnetized, the temperature decreases due to the magnetocaloric effect, and the cycle repeats

Figure 2-3 shows the assumed refrigerant cycle occurring in the differential section at some location in the AMR. The cycle as described above is equivalent to the process starting at point '*a*' and proceeding alphabetically to return to the starting point.

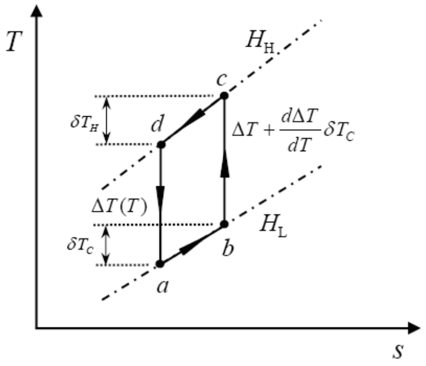

Figure 2-3. Hypothetical cycle for the magnetic refrigerant at some cross-section of the AMR [3].

It is assumed that the magnitude of the MCE for the process b-c is described by a first order Taylor series approximation in reference to point a. In the reversible case, the resulting area within the T-s diagram is equivalent to the magnetic work input per unit mass for a complete cycle.

If the details of the AMR are ignored and one focuses on the absorption of heat by the fluid flowing through the cold reservoir, the cooling power can be determined from,

$$\dot{Q}_c = \oint \dot{m}_f(t) c_p T_f(t) dt \tag{2.9}$$

where $\dot{m}_f(t)$ is the fluid mass flow rate as a function of time, c_p is the fluid heat capacity, and T_f is the fluid temperature at the exit of the AMR. For a complete cycle the integral can be written as,

$$\dot{Q}_c = (m_f c_p)\Delta T_f \tag{2.10}$$

where ΔT_f is the effective temperature change of the fluid as it flows through the cold heat exchanger, and m_f is the mass of fluid that flows through the AMR when it is demagnetized. If the regenerator has a very high number of thermal transfer units (NTU), the temperature of the fluid exiting the AMR will closely match the temperature of the solid refrigerant at the cold end. In addition, if the thermal mass of the refrigerant is much greater than the thermal capacity of the total fluid flux through the regenerator, the temperature of the solid will not change much. The ratio of the fluid thermal capacity to the regenerator thermal mass is called the utilization and is defined as,

$$\Phi = \frac{m_f c_p}{M c_b} \tag{2.11}$$

where M is the mass of refrigerant in the regenerator and c_B is the heat capacity of the refrigerant taken at a reference point (often at T_{curie}, $H=0$). In the limit of very small utilization and large NTU, and assuming parasitic heat leaks are insignificant, the temperature change of the fluid as it absorbs heat through the cold heat exchanger is equal to the magnetocaloric effect of the refrigerant at the cold end of the regenerator, $\Delta T_f = \Delta T_C$. In terms of passive regenerators, Φ is sometimes referred to as the matrix capacity rate ratio and varies little throughout the regenerator for constant fluid heat capacity. For an AMR, the local utilization is a function of field and temperature and, in general, is position dependent.

If the AMR cycle is a reversible process, no entropy is generated in the regenerator, and therefore the same amount of entropy flows in and out. In addition, if the regenerator is assumed to behave as a cascade system of an infinite number of magnetic refrigerators the following relation is true throughout the regenerator length [17]:

$$\dot{S}(x) = \frac{\dot{Q}(x)}{T(x)} = const \tag{2.12}$$

where $\dot{S}$ and $\dot{Q}$ are the entropy and heat flow rate and T is the absolute temperature, all at the same axial location x. Furthermore, the boundary conditions at the hot and cold end are:

$$\dot{Q}_c = \dot{m}_f c_p \Delta T_{ad_c} \tag{2.13}$$

$$\dot{Q}_h = \dot{m}_f c_p \Delta T_{ad_h} \tag{2.14}$$

Thus, substituting (2.13) and (2.14) into (2.12) we obtain

$$\frac{\Delta T_{ad_c}}{T_c} = \frac{\Delta T_{ad_h}}{T_h} \qquad (2.15)$$

Lastly, if we consider the temperature of the hot end the reference temperature, the above expression suggests that the magnetocaloric effect must scale with temperature according to the following relation:

$$\Delta T_{ad}^{ideal}(T) = T\frac{\Delta T_{ref}}{T_{ref}} \qquad (2.16)$$

where ΔT_{ad}^{ideal} is the ideal MCE at temperature T, ΔT_{ref} is the MCE at the hot end of the AMR, and T_{ref} is the temperature of the AMR at the hot end in the low magnetic field. Equation (2.16) states the ideal magnetocaloric effect should be a linearly increasing function of temperature. If correct, this expression implies that if the magnetocaloric effect at the cold end of the AMR exceeds that at the hot end, the second law of thermodynamics will be defied [3]. This constraint has led researchers to search for magnetic refrigerants that match this linear expression for MCE.

It has been argued that even though comparing an AMR to a cascade of refrigerators helps in understanding the AMR cycle, the analogy does not strictly apply [17]. More specifically, the interactions among the infinitesimal AMR layers are complex, nonlinear and marginally understood. As a consequence the validity of Equation (2.16) is questionable, and it can only be used as a guideline.

Because the adiabatic temperature change is temperature dependant, the MCE is a function of position in a regenerator. Consequently in order to predict the adiabatic temperature change at a specific location *x*, it is necessary to know the temperature at this location. For passive regenerators the temperature profile is nearly linear, with a small deviation at the ends [17]. The same cannot be assumed for AMRs, especially if a high utilization factor is used.

Current multi-material AMR data also shows that the temperature profile can significantly deviate from linear depending on operating heat rejection temperature, underlying the complexity of the interaction of the temperature profile with the local MCE. Such interdependency suggests another possible issue with multi-material regenerators: initial condition sensitivity. Assuming that an AMR starts operating with a uniform temperature of $T = T_H$, it will eventually reach a pseudo steady state temperature distribution. At the beginning of the process, cooling is almost entirely performed by the hot end layer, which is already within its MCE operating temperature range (assuming that the materials have significantly different Curie temperatures). As a temperature gradient starts to develop, the other layers begin contributing to the overall refrigeration process, until a steady state temperature profile is established. The larger the final temperature span, the further away the cold end is from its MCE operating range at the beginning of the process. Thus, it is possible that when starting from a temperature profile $T(x) = T_H$, there is not enough cooling power to drive the AMR to the expected operating regime. It could then be necessary to pre-cool the cold end to "prime" the regenerator. In this case the AMR could have two or more operating regimes depending on the initial conditions.

Governing equations for an AMR system have been developed throughout the years with the objective of analytically or numerically describe its thermo-magnetic state at a specific time and for a given set of boundary conditions. They consist of a system of two equations, one for the fluid and the other for the solid matrix. These equations are derived from the energy balance expressions for each phase. Since they are coupled, they must be solved simultaneously.

The energy balance for a heat transfer fluid flowing through a regenerator can be summarized by the following [18]:

$$\rho_f c_p A_f \frac{\partial T_f}{\partial t} = -\dot{m}_f c_p \frac{\partial T_f}{\partial x} + \frac{\partial}{\partial x}\left(k_f A_f \frac{\partial T_f}{\partial x}\right) + hP_w\left(T_s - T_f\right) + \left|\frac{\partial p}{\partial x}\frac{\dot{m}}{\rho_f}\right| \tag{2.17}$$

where ρ_f is the density, A_f is the area of fluid flow, k_f is the thermal conductivity, h is the convection heat transfer coefficient, P_w is the wetted perimeter, or cross-sectional contact area between the fluid and the regenerator matrix, and p is the fluid pressure. All parameters with the subscript f refer to the fluid. The viscous losses are a function of the pressure drop $\frac{\partial p}{\partial x}$, which strongly depends on the operating frequency and system pressure. Pressure drop sets a major limitation on AMR efficiency, thus, much work is focused on its minimization through the choice of heat transfer fluid, regenerator matrix microscale structure, and AMR aspect ratio.

Similarly the energy balance for the solid matrix can be expressed as it follows [18]:

$$\rho_s A_s \left(\frac{\partial u_s}{\partial t} - B\frac{\partial m}{\partial t}\right) = \frac{\partial}{\partial x}\left(k_s A_s \frac{\partial T_s}{\partial x}\right) + hP_w\left(T_f - T_s\right) \qquad (2.18)$$

where the magnetic work term has been grouped on the left side of the expression with the internal energy term. Both the fluid and matrix expressions assume uniform properties in the radial direction and adiabatic cylindrical walls. In Equation (2.18) the dissipation terms are not present, however there is an additional magnetic work term. The Equation (2.17) can be expressed as [18]:

$$k\frac{\partial T_f}{\partial t^*} = -\Phi\frac{\partial T_f}{\partial x^*} + \frac{\partial}{\partial x^*}\left(\frac{\varphi}{Pe_f}\frac{\partial T_s}{\partial x^*}\right) + NTU\Phi(T_s - T_f) \qquad (2.19)$$

where the following non-dimensional parameters have been introduced:

$$\Phi = \frac{\dot{m}_f c_p \tau}{M_s c_B} \qquad (2.20)$$

$$NTU = \frac{hA_w}{\dot{m}_f c_p} \qquad (2.21)$$

$$k = \frac{M_f c_p}{M_s c_B} \qquad (2.22)$$

$$Pe_f = \frac{\dot{m} c_f L}{k_{eff} A_f} \qquad (2.23)$$

$$t^* = \frac{t}{T};\ x^* = \frac{x}{L} \qquad (2.24)$$

where A_w is the wetted area, M_f the mass of the gas within the regenerator, L length of the regenerator, and k_{eff} is the conductivity of the regenerator and fluid, taking into account dispersion effects.

Chapter 3

Thermal Regenerators

A regenerator is often viewed as a regenerative heat exchanger. In an ordinary heat exchanger, the two fluids exchanging energy are separated by a solid surface. In a regenerator, the same space is occupied alternately by the hot fluid and the cold fluid while the energy to be transferred is stored and released from the regenerator packing material (matrix). The hot fluid and cold fluid only differ in temperature and pass in periodical operation through the regenerator matrix. As the hot fluid passes through the permeable regenerator matrix thermal energy is stored in the solid material. This sequence of operation is referred to as the hot blow or hot period. During the cold blow or cold period the flow is reversed and the stored energy is recovered by the cold fluid (entering from a cold reservoir) and rejected to the hot space [19].

The first technical application that made use of regenerators might be the Stirling engine. In a two cylinder type Stirling engine the two cylinders are connected using a regenerator. The regenerator periodically stores the energy that is displaced from either the hot or the cold cylinder. Without the regenerator the stored amount of thermal energy would be irreversibly rejected to the environment and thus lowering the efficiency of the device significantly. In this sense the regenerator acts to maintain the temperature span between the two cylinders. GM and thermoacoustic cryocoolers also relay on regenerators, where use of a helium compression cycle coupled with highly effective regenerators allows cooling down to 2.5 to 3 K.

The research and results that are presented in this work are mainly used for the design of new potential regenerator geometries to be used in AMRR prototypes. However, because of the broad range of applications of regenerators in thermal devices, the methodology and results can be adapted to similar devices with similar operating conditions.

3.1 Thermohydraulic Optimization of Regenerators

Multiple transport processes take place in an AMR. Among the most basic ones is the transport of momentum and thermal energy. Thus the thermohydraulic optimization of an AMR can be done in a passive environment (i.e. in the absence of any magnetic field). The properties of a well-designed passive regenerator are [20]:

1. High heat transfer (product of interfacial heat transfer coefficient times interfacial area). Favorable geometries are packed beds, parallel channels, rectangular channels or perforated plates.
2. Large thermal mass of the regenerator material compared to the heat transfer fluid.
3. Small axial thermal conduction in both regenerator and heat transfer fluid. In contrast, the radial conductivity should be high to maintain internal equilibrium. These two properties can only be guaranteed by a choice of a proper geometry (i.e. the geometry should introduce more thermal resistance in the axial than in the radial direction).
4. Low pressure drop to minimize irreversible pumping losses.
5. Low dead volume associated with the porous structure of the regenerator. Actual void to total volume ratio ranges between 0.3 and 0.7. In an AMR, the fluid in the void spaces acts as a parasitic load, decreasing the useful magnetocaloric effect.

Many of these characteristics are typically opposing each other, for example large heat transfer area, and small dead volume result in high pressure drops across the regenerator. Thus this optimization problem is not trivial and has been a challenge to many thermal engineers in the past. For this reason, passive regenerator testing and modeling is a research topic with a long history. One of the primary goals in this field is to determine friction factor and interfacial heat transfer coefficient of the regenerator matrix.

So far, it has proven difficult to generalize results. The actual performance depends on a large parameter space resulting in large scattering in the heat transfer coefficient. As a result, it becomes essential to characterize a regenerator geometry within the aspect ratios and operating conditions needed for a particular device.

For this reason a passive regenerator test apparatus (PRTA) has been developed to gain further understanding of the thermal and hydraulic properties of a certain regenerator geometry. The outcome of an experiment using this apparatus is typically a correlation for the heat transfer coefficient (or Nusselt number) and the friction factor as a function of operating condition and regenerator design. The Nusselt number describes the ratio between convective and conductive heat transfer. The friction factor represents the non-dimensional pressure drop through the regenerator.

The use of these correlations is twofold. The correlations are used to determine the amount of energy dissipation that a certain regenerator geometry involves. Based on this criteria (and other non thermohydraulic properties), a regenerator can be used in a prototype that shows optimal heat transfer to pressure drop ratio. In addition, the correlations can be used for high level models that predict gross power output and temperature span in an actual device. The Nusselt number is of particular interest as the performance of many regenerative devices is very sensitive to this parameter. As result, model predictions are greatly improved by having accurate information regarding the heat transfer of a given regenerator matrix.

3.2 Passive Regenerator Testing

Passive testing involves characterization of regenerator geometries in absence of a magnetic field. As a result, the regenerators for passive testing can be made of a metal that has much better availability at lower prices but has similar properties (i.e. density, heat capacity, thermal conductivity) compared to an active magnetic material.

Regenerator testing for design optimization can be summarized in the following phases. At first there is an initial idea of a potential geometry. This originates from either experience or initial model predictions. Once test data has been collected, the data is analyzed and useful information like Nusselt number is extracted. The plausibility of the results is validated with independent simulations and/or comparing to existing correlations' outcomes. After some iterations the geometry can be compared to previously tested structures. In this way, preferred geometries can be fabricated using active magnetic materials and thus allows for testing in AMRR prototypes. However, it must be pointed out that a well performing passive geometry might be infeasible for active magnetic use, because it enhances magnetic losses, like strong demagnetizing effects or eddy current dissipation.

3.3 Previous Work and Literature Review

Regenerators are key components of many different thermal devices, and thus have been studied for many years. Many excellent references are available, e.g. Schmidt and Wilmott [19], [21],[22]. Research on regenerators has many different facets; much of the experimental work falls into the cryogenic regime, where the regenerator is used in Stirling cryocoolers. Typically these devices utilize a gas as working fluid which is very different from the present experimental conditions. Hence, these references are only of conceptual use for the present work. Most of the hydraulic and thermal characteristics of regenerators are studied within the more general concept of porous media. There is a large number of publications that concerns thermal energy and momentum transport through porous media. Many studies are limited to porous media in form of packed particle beds because of their high interfacial area. Wakao and Kaguei [24] presented a comprehensive review on techniques for the extraction of the heat transfer coefficient. They found significant scattering of the resulting correlations for the Nusselt number especially at low Reynolds number flows. Achenbach [25] points out in his review, that the large parameter space for the Nusselt number is responsible for large experimental scattering. Hence, the various experimental conditions can not be generalized to represent the Nusselt number in an infinitely packed porous bed. Achenbach [7] points out that the ratio of hydraulic diameter to regenerator diameter and the non-uniform void distribution in the radial direction (channeling) are often not considered in the experimental determination of the Nusselt number.

Another point that must be considered is what thermal transport phenomena have been taken into account for the determination of the Nusselt number. Hsu [26] gives an excellent review for the use of macroscopic transport equations derived from volume averaging techniques. The closure of these equations requires additional terms in the energy balance: interfacial heat transfer (constituted by the Nusselt number), thermal dispersion and thermal tortuosity. In addition, effective thermal conductivities appear in the balance equations from volume averaging. In theory, all these "new" macroscopic transport processes described by constitutive relations must be determined experimentally. A simultaneous determination of the closure coefficients is unlikely. Hence, single experiments must be carried out to determine the coefficient in question. For particle beds, the correlation presented by Wakao and Kaguei [24] evolved as a benchmark and is often used for modeling and simulation of particle beds. In their work they included thermal dispersion in the energy balance to extract the Nusselt number. Often thermal turtuousity is not considered at all. Another approach is chosen by Hausen [26], he neglected conductive transport completely (and therewith thermal dispersion) and came up with a bulk heat transfer coefficient that embodies interfacial heat transfer and resistance to heat transfer within the regenerator packing and the fluid. Thus, it is not surprising that the different models used to extract heat transfer data will amplify the scattering in Nusselt number predictions.

Recently, Engelbrecht [28] came up with a new Nusselt number correlation for packed bed of spheres with diameter of 4mm. He investigated the heat transfer using water and water-glycol mixtures as heat transfer medium. The regenerator dimensions are very similar to the present work. He found that his new correlation significantly under predicts the Wakao correlation (derived for gaseous heat transfer fluids). He also found a large experimental uncertainty of the Nusselt number which is amplified by the temperature dependence of Reynolds and Prandtl number. His correlation turned out to be close to the one presented by Macias-Machin et al [29] who investigated Nusselt number for liquid heat transfer fluids only.

It must be pointed out that all the work reviewed to this point corresponds to the so called “single-blow“ technique. In this technique the regenerator is fluidized at a constant flow rate. At the beginning of the experiment the regenerator is subjected to a quasi-step change in temperature. Simultaneously, the temperature is recorded downstream of the regenerator. The temperature residual of model and experiment downstream of the regenerator is minimized by an appropriate choice of the heat transfer coefficient determined by a least square estimator. This method only approximates the heat transfer in regenerators since the flow in thermal regenerator operation is oscillating.

None of the previously reviewed papers discusses the effects of an oscillating flow which represents a typical operating condition of many thermal devices using a regenerator. Many studies deal with the analysis of heat transfer under oscillating flow conditions in channels and pipes without porous media.

Lee et al [30] presented an experimental study of oscillating flow in wire mesh regenerators. Their study compares regenerators with different wire mesh numbers but the same porosity. Their experimental set up is very similar to the one presented in this thesis. However, the fact that they used a gaseous heat transfer fluid does not allow for a direct comparison to experimental situations with incompressible flow as investigated in this thesis. They measured temperatures and pressure losses between frequencies of 1-10 Hz at a fixed stroke. They placed three thermocouples inside the regenerator and two outside. They measured negligible temperature oscillations inside the regenerator and attributed this finding to the low stroke, the compressibility of the gas and the regeneration effect. They also showed that a regenerator made up of a combination of wired mesh using different mesh numbers can increase the effectiveness of the regenerator. However, they do not show a correlation for the Nusselt number.

Daney [31] compared ineffectiveness of parallel plates, screens and spheres regenerators in oscillating flow to a square-wave mass flow form. He modified effectiveness values for constant mass flow rates to oscillating flow situations. For all regenerator geometries, he found an increase of ineffectiveness when sinusoidal flow is used. However, it is difficult to draw strong conclusions from this because of the simplified model he used. In fact, he assumed infinite thermal mass of the regenerator and in-phase evolution of the Nusselt number with respect to the mass flow.

The work of Chen et al [32] is dedicated to the analytical calculation of the Nusselt number for a gaseous flow through a parallel plate or circular tube regenerator in an oscillating flow. They assumed a periodic form for the velocity, temperature and pressure field and found closed form solutions for the complex Nusselt number. The calculation is executed on a representative element of the channel (i.e. a single channel or tube). They also neglected temperature oscillations in the matrix (infinite thermal mass of the regenerator material). The Nusselt expression obtained is decomposed in two contributions; one due to a mean temperature gradient present, the other due to the compressibility of the gas. In the low frequency range, they obtained Nusselt numbers for parallel plates Nu ≈ 10 and for circular tubes Nu ≈ 6.

An excellent review of oscillating flow in Stirling engines is given by Simon and Seume [33]. Their survey discusses the use of proper similarity parameters for oscillating flow as for example the kinetic Reynolds number (dimensionless frequency). The differences between steady flow and oscillating flow are illustrated for the flow in a pipe. A parabolic velocity profile is found when the flow is steady or at low oscillating frequency. As the frequency increases and annular effect is observable where the velocity peaks close to the wall. They stress that there is no clear indication for the transition from laminar to turbulent flow in porous media under oscillating flow conditions.

A study that falls in the category of oscillatory heat transfer in plain media was presented by Zhao and Cheng [34]. They experimentally and numerically investigated the heat transfer in a heated pipe subjected to oscillatory flow. A constant heat flux is applied to the pipe using an insulated flexible heater wrapped around the pipe wall. They found good agreement between the model and temperature measurements at different axial positions (center line of the pipe) as well as in the fluid pipe. They showed that the fluid temperature oscillations are smaller at the center axial positions than at the ends of the pipe. At the axial center position of the pipe wall the temperature oscillations become vanishingly small. They obtained a Nusselt number correlation that is monotonically increasing in both frequency and stroke. In the low stroke and low frequency range, they predicted a Nusselt number of 0.6 and in the high frequency (10 Hz) /high stroke range a Nusselt number of 12.5.

It can be concluded that heat transfer in regenerators is typically analyzed under steady flow conditions using a gas as heat transfer medium. Oscillating flow type heat transfer using a high density fluid (such as water) has been studied theoretically or experimentally but not combined. The experimental work reviewed is limited to the presentation of raw experimental data without presentation of meaningful dimensionless groups such as Nusselt number and friction factor. On the other hand, the theoretical work lacks experimental justification.

This work presents both experimental and theoretical analysis as well as the representation of pressure drop and heat transfer coefficients in terms of dimensionless numbers.

Chapter 4

Macroscopic Balance Equations

4.1 Regenerator Disposition

The regenerator is embedded in a hydraulic circuit as shown in Figure 4-1.

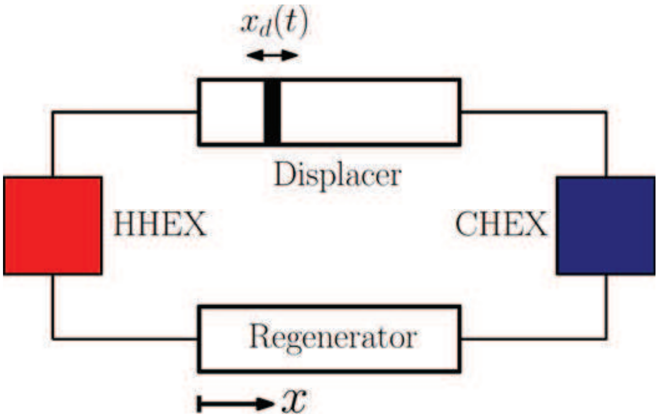

Figure 4-1: Regenerator situation in hydraulic circuit

Layout depicted in Figure 4-1 represents the experimental configuration covered in chapter 6.1. The two heat exchangers are sinked to a heater and chiller respectively and impose a temperature gradient across the regenerator. The displacer produces periodic mass flow at any point in the circuit. The following sections focus on mathematical description of the transport processes in the regenerator.

4.2 Length Scales and Volume Averages

Regenerators can be understood as porous media. The existence of at least two different length scales is characteristic for these media: the typical diameter of the pores d and the device length L as illustrated in Figure 4-2.

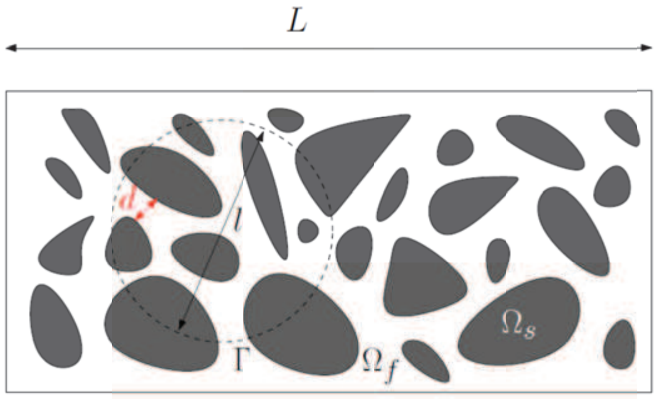

Figure 4-2: Schematic of porous media

In practice, the pore characteristic dimension can be $d \approx 100$ µm while the device length may be $L \approx 10$ cm or longer. An attempt to solve the governing equations for the whole device length resolved on the pore scale is not recommendable. An immense computational effort would be needed to specify a computational grid and boundary conditions for the regenerator. The solution to this problem is the description of physically relevant fields only on an average basis. The approach presented in [36] deduces effective transport equations for suitably defined volume averages of the true physical quantities. Any physical quantity ψ (tensor of any order) can be averaged over a representative elementary volume (*REV*) denoted V_Γ:

$$\langle\psi\rangle = \frac{1}{V_\Gamma}\int_\Gamma \psi dV. \tag{4.1}$$

The local *REV* V_Γ is chosen such that it is the smallest differential volume that results in statistically meaningful local average properties. In regenerators, the pore scale is much smaller than the device scale (the regenerator length L_r) $d << L_r$. Hence the variation of a physical quantity across the pore scale is negligible compared to the variation across the device length. So we are free to choose the size of a *REV* such that its scale is larger than the pore scale, but smaller than the device scale.

$$d \ll l \ll L_r \tag{4.2}$$

An example to locally averaged quantity is the superficial (or Darcian) velocity

$$\langle v \rangle \equiv v_s = \frac{1}{V_\Gamma} \int_\Gamma v(x) dV \tag{4.3}$$

Another example is the porosity. The porosity can be calculated by introducing a void distribution function [20]

$$a(x) = \begin{cases} 1 & x \in \Omega_f \\ 0 & x \in \Omega_s \end{cases} \tag{4.4}$$

where Ω_f and Ω_s denote the fluid and solid domain as indicated in Figure 4-2. These two domains build the whole regenerator domain $\Omega_r = \Omega_f \cup \Omega_s$. The local average porosity is the average of the void distribution function

$$\varepsilon(x) = \frac{1}{V_\Gamma} \int_\Gamma a(x) dV \tag{4.5}$$

Hence, the bulk porosity is obtained by setting the *REV* equal to the regenerator volume $V_\Gamma = V_r$. Then equation (4.5) becomes

$$\varepsilon = \frac{1}{V_r} \int_{\Omega_r} a(x) dV = \frac{1}{V_r} \int_{\Omega_f} dV = \frac{V_f}{V_r}. \tag{4.6}$$

With the definition of the porosity we can also average any physical quantity over the fluid or solid phase only, a so called intrinsic average

$$\langle \psi \rangle^f = \frac{1}{V_{\Gamma_f}} \int_{\Gamma_f} \psi dV = \frac{\langle \psi \rangle}{\varepsilon} \tag{4.7}$$

where the volume occupied by the fluid within Γ is denoted by $V_{\Gamma f} = \int_\Gamma a(x) dV$. As an example we consider the pore velocity as an intrinsic average

$$\langle v \rangle^f \equiv v_p = \frac{1}{V_{\Gamma_f}} \int_{\Gamma_f} v(x) dV = \frac{v_s}{\varepsilon} \tag{4.8}$$

4.3 Macroscopic Balance Equations

The macroscopic balance equations are obtained by volume averaging the microscopic transport equations. We constrain the analysis by reducing the equations for one dimensional flow and heat transfer in axial direction x.

4.3.1 Macroscopic Thermal Energy Balance

The regenerator can be seen as an isolation of two different temperature levels, resulting in a temperature gradient across the regenerator. The matrix of the regenerator serves as periodic thermal storage device as it absorbs and expels heat to the heat transfer fluid. The oscillating fluid flow is divided in two periods referred to as hot and cold period. During the hot period, the fluid flow is from the hot to the cold side of the regenerator during which the matrix absorbs and stores the heat of the fluid. In the reverse flow direction the stored heat is transferred back to the fluid, referred to as cold period. One hot and cold period corresponds to a full cycle. The temperature profile across the regenerator repeats for a full period as soon as the system reaches steady state condition.

Ideal Regenerator

First, the ideal operation of a regenerator is discussed. This theoretical performance would be reached with the following properties of the regenerator process:

- infinite thermal mass,
- infinite heat transfer area,
- no longitudinal conduction and
- no pressure drop.

Under these ideal conditions, illustrated in Figure 4-3, the fluid enters the regenerator at the hot temperature $T_{h,in}$ during the hot blow, heats the solid matrix and exits at a cooler temperature $T_{h,out}$. The opposite occurs during the cold blow, the solid matrix heats the cold fluid which enters with the cool temperature $T_{c,in}$ and exits at a higher temperature $T_{c,out}$.

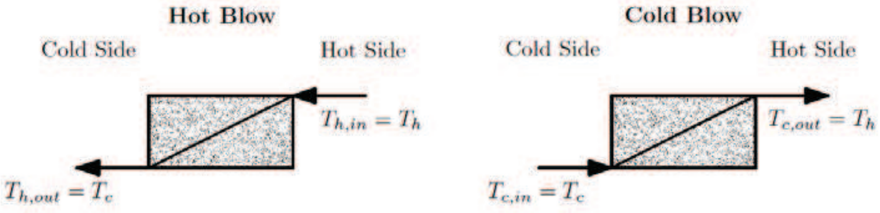

Figure 4-3: Hot and cold blow for an ideal regenerator.

Particular for the ideal case is the equality of the outlet temperatures to the corresponding inlet temperatures, i.e., the exit temperature $T_{h,out}$ is equal to the inlet temperature at the cold side $T_{c,in}$ and according to that the outlet temperature $T_{c,out}$ is equal to the inlet temperature $T_{h,in}$ at the hot side. Also, for the particular case of the ideal regenerator, the temperature distribution across the regenerator is constant (as shown in Figure 4-3). The real regenerator processes are designed as close as possible to this lossless ideal scenario in order to maximize the regenerator performance.

Real Regenerator

In the real regenerator process, longitudinal conduction, finite thermal mass, finite heat transfer and pressure drop reduce the effectiveness. The cyclic operation of a real regenerator is shown in Figure 4-4.

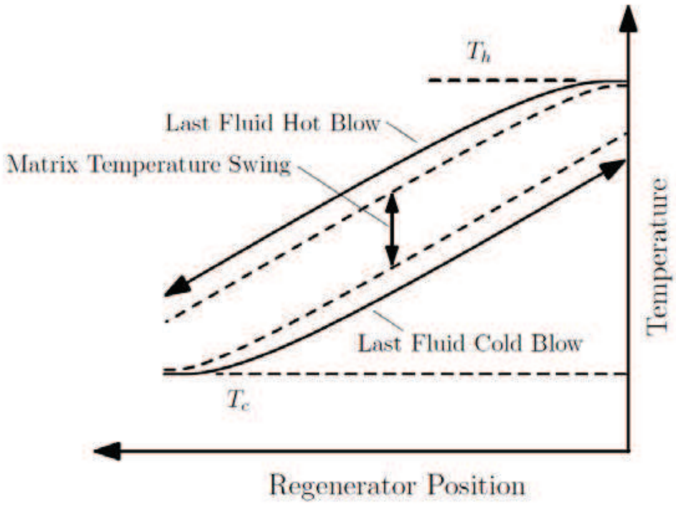

Figure 4-4: Hot and cold blow for a real regenerator.

The real conditions cause that the matrix to not completely absorb the full amount of heat energy required to maintain a perfect buffer between the hot and cold temperature levels. Thus, the fluid is cooled by the matrix to a higher value than the temperature at the cold side T_c during the hot blow. Similarly, the outlet temperature of the cold blow is lower than the hot side temperature T_h. Thus the temperature swing of the matrix is lower compared to the temperature swing of the fluid because of the finite heat transfer.

Schumann model

This is the simplest of all models. Axial thermal conduction is neglected in both phases and no viscous dissipation is taken into account. Also the effect of thermal turtuosity is neglected completely. The Schumann model is given by the two thermal balance equations, the first one for the fluid, and the second one for the solid:

$$\frac{\partial T_f}{\partial t} = -v_p \frac{\partial T_f}{\partial x} + \frac{h a_{sf}}{\varepsilon(\rho c)_f}\left(T_s - T_f\right) \tag{4.9}$$

$$\frac{\partial T_s}{\partial t} = -\frac{h a_{sf}}{(1-\varepsilon)(\rho c)_s}\left(T_s - T_f\right) \tag{4.10}$$

where h is the heat transfer coefficient, ρ is density, c is specific heat, T is temperature and a_{sf} is the specific surface area. The subscripts f and s stand for fluid and solid respectively. For a simplified notation $\langle T\rangle^f = T_f$, $\langle T\rangle^s = T_s$ is used. The advantage of this model is that h is the only unknown which must be determined experimentally. It is assumed that h also includes thermal dispersion, turtuosity and other effects which are not captured by the model.

Continuous solid model

In this model the axial conduction, in both phases, is included through the use of effective thermal conductivities κ_f^{eff}, κ_s^{eff}. The effective thermal diffusivity for phase k is $\alpha_k^{eff} = \kappa_k^{eff}/(\rho c)_k$:

$$\frac{\partial T_f}{\partial t} = -v_p\frac{\partial T_f}{\partial x} + \alpha_f^{eff}\frac{\partial^2 T_f}{\partial x^2} + \frac{h a_{sf}}{\varepsilon(\rho c)_f}\left(T_s - T_f\right) \tag{4.11}$$

$$\frac{\partial T_s}{\partial t} = \alpha_s^{eff}\frac{\partial^2 T_s}{\partial x^2} - \frac{h a_{sf}}{(1-\varepsilon)(\rho c)_s}\left(T_s - T_f\right). \tag{4.12}$$

In general, the thermal conductivities are unknown and depend on the geometrical configuration and the material used. They can be obtained from correlations available in literature or from detailed simulations. Wakao and Kaguei [24] also include dispersion in κ_f^{eff}. The incorporation of dispersion will result in a velocity dependency of κ_f^{eff}. However, the model comprises additional unknowns $\kappa_f^{eff}, \kappa_s^{eff}$, which must be either determined experimentally or taken from correlations available in literature. Viscous dissipation and ambient heat loss are also neglected in this model.

4.3.2 Fluid Velocities

The source of the fluid flow is the motion of the displacer, which undergoes harmonic oscillation. The time-dependent displacer position $x_D(t)$ given by:

$$x_D(t) = \frac{S}{2}\sin(\omega t) \tag{4.13}$$

The time-dependent sinusoidal wave is characterized by half stroke S as amplitude and the angular frequency ω multiplied with time t as phase. The cycle duration for one full period T_{fp} is determined by:

$$T_{fp} = \frac{1}{f} \tag{4.14}$$

With f frequency. The fluid velocity in the displacer is equal to the velocity of the displacer $u_D(t)$ and is calculated by the time derivative of Equation 4.13 and leads to:

$$v_D(t) = \frac{S}{2}\omega\cos(\omega t) \tag{4.15}$$

Thus, the fluid velocity is 90º phase-delayed to the position of the displacer. This fluid velocity can be also expressed as the volumetric flow rate $\dot{V}_D(t)$ divided by the cross-sectional area of the displacer A_D:

$$v_D(t) = \frac{\dot{V}_D}{A_D}\omega\cos(\omega t) \tag{4.16}$$

Using Equation 4.8 for which the pore velocity $v_p = v_s/\epsilon$ and defining the regenerator cross-sectional area as A_R, whe have:

$$v_p(t) = \frac{1}{\epsilon}\frac{A_D}{A_R}\frac{S}{2}\omega\cos(\omega t) \tag{4.17}$$

which gives the peak pore velocity:

$$v_p^{max} = \frac{1}{\epsilon}\frac{A_D}{A_R}\frac{S}{2}\omega \tag{4.18}$$

4.3.3 Macroscopic Momentum Balance

Conservation of momentum of a fluid passing thorugh a porous medium is described by Darcy's law and it is analogus to the Fourier law for heat conduction, or Ohm's law for electrical currents, or for or Fick's law for difffusion. They all have in common a driving force based on a gradient, a resistance, and a flux.

$$\dot{V} = \frac{-kA}{\mu}\frac{(\Delta P)}{L} \tag{4.19}$$

The total volume flow rate $\dot{V}$ is the product of the permeability k, the cross sectional area of the flow A and the pressure drop ΔP, and it is inversely proportional to the viscosity μ. A more general notation is:

$$v_p = -\frac{k}{\mu}\nabla P \tag{4.20}$$

Where v_p is the pore velocity and ∇P is the pressure gradient.

4.3.4 Dimensionless Parameters

Standard thermo-hydraulic groupings are presented in this section that lead to suitable standardization of experimental data and the governing equations.

The hydraulic diameter standardizes the flow in an arbitrary duct. The hydraulic radius is proportional to the ratio of free flow cross sectional area A_f and wetted perimeter P_w. This ratio can be extended to a volumetric ratio, namely the ratio of entrained fluid volume V_f in the pores to interfacial surface area ($A_{sf} = a_{sf}V_r$) available for heat transfer.

$$d_h = 4\frac{A_f}{P_w} = 4\frac{V_f}{a_{sf}V_r} = \frac{4\varepsilon}{a_{sf}} \tag{4.21}$$

Similarly, the characteristic length with respect to the packing material is defined as

$$l_c = \frac{V_s}{a_{sf}V_r} = \frac{1-\varepsilon}{a_{sf}} \tag{4.22}$$

The ratio of hydraulic radius and characteristic length is a function of porosity only

$$\frac{d_h}{l_c} = 4\frac{\varepsilon}{1-\varepsilon} \tag{4.23}$$

The ratio of original coordinate to hydraulic diameter is chosen as dimensionless length

$$\xi = \frac{x}{d_h} \tag{4.24}$$

The dimensionless time is scaled with the angular frequency

$$\hat{t} = \omega t \tag{4.25}$$

The instantaneous velocity is scaled with the peak pore velocity

$$\hat{v} = \frac{v}{v_{p1}} \tag{4.26}$$

where v_{p1} is the peak pore velocity. The pressure is non-dimensionalized with respect to dynamic pressure, i.e.

$$\hat{p} = \frac{p-p_0}{\rho v_{p1}^2} \tag{4.27}$$

The pressure gradient is accordingly,

$$\frac{\mathrm{d}\hat{p}}{\mathrm{d}\xi} = \frac{d_h}{\rho v_{p1}^2}\frac{\mathrm{d}p}{\mathrm{d}x} \tag{4.28}$$

The friction factor relates the pressure loss of a porous medium to the average velocity. The Darcian friction factor is given by

$$f_D = \frac{d_h}{2}\frac{\frac{\mathrm{d}p}{\mathrm{d}x}}{\rho v_{p1}^2} \tag{4.29}$$

The friction factor is twice the dimensionless pressure gradient

$$f_D = 2\frac{\mathrm{d}\hat{p}}{\mathrm{d}\xi} \tag{4.30}$$

The peak Reynolds number based on hydraulic diameter relates inertial forces and viscous forces

$$Re_{dh} = \frac{\rho_f v_{p1} d_h}{\mu_f} \tag{4.31}$$

where v_{p1} is the pore velocity to first order (i.e. the peak pore velocity). The peak velocity can reach the same value for a low frequency/ high stroke and high frequency/low stroke configuration. The kinetic Reynolds number is a dimensionless expression for the oscillating inertial forces in relation to viscous forces.

$$Re_\omega = \frac{\rho_f \omega d_h^2}{\mu_f} \tag{4.32}$$

More commonly used for the description of oscillating flow is the Womersley number $\mathrm{Wo} = \sqrt{\mathrm{Re}_\omega}$. Under higher frequencies where Re_ω and Wo are large, viscous forces become less important resulting in plug like flow. Under small frequencies the flow might deviate from the plug profile since the flow has time to develop a flow profile within a cycle. The kinetic Reynolds number can also be considered as a non dimensional frequency. Beside frequency, the stroke of the displacer can also be controlled. The non dimensional displacement is given by the ratio of stroke L_s and hydraulic diameter.

$$A_0 = \frac{L_s^{eff}}{2\varepsilon d_h} = \frac{L_s}{2\varepsilon d_h}\frac{A_{eff}}{A_r} \tag{4.33}$$

Here the effective stroke takes into account the different cross sectional areas of displacer A_{disp} and the regenerator A_r. Using these definitions the peak Reynolds number, kinetic Reynolds number and non dimensional amplitude relate to

$$Re_{dh} = \mathrm{Re}_\omega \cdot A_0 \tag{4.34}$$

The Nusslet number is the ratio of convective thermal energy transfer to conductive energy transport

$$Nu = \frac{h \cdot d_h}{\kappa_f} \tag{4.35}$$

Similarly, the heat transfer coefficient can be non-dimensionalized with respect to conductive energy transport in the packing material, known as Biot number

$$Bi = \frac{h \cdot l_c}{\kappa_s} \tag{4.36}$$

The Prandtl number is the ratio of viscous diffusion to thermal diffusion.

$$Pr = \frac{c_f \mu_f}{\kappa_f} \tag{4.37}$$

The Fourier number is conceptually the ratio of the heat conduction rate to the rate of thermal energy storage, i.e. Fo $= \alpha_s t_0 / l_c^2$, where t_0 is a characteristic time scale. In oscillating flow it is reasonable to pick $t_0 = 1/\omega$. The Fourier number is

$$Fo = \frac{\alpha_s}{l_c^2 \omega} \tag{4.38}$$

The ratio of the intrinsic thermal conductivities of both phases is defined as

$$\gamma_k = \frac{\kappa_f}{\kappa_s} \tag{4.39}$$

The ratio for fluid to solid thermal mass is

$$R = \frac{\varepsilon}{1-\varepsilon} \frac{(\rho c)_f}{(\rho c)_s} \tag{4.40}$$

The thermal mass ratio can be related to a combination of the present groupings as

$$R = \frac{Pr Re_\omega Fo Bi}{4Nu} \tag{4.41}$$

The ratio of Nusselt to Biot number is

$$\frac{Nu}{Bi} = \frac{d_h}{l_c} \frac{1}{\gamma_k} = \frac{4\varepsilon}{1-\varepsilon} \cdot \frac{1}{\gamma_k} \tag{4.42}$$

Chapter 5

Heat Transfer Coefficient Determination

5.1 Analytical Model

The basic equations for the model consider the first-law energy balance on an infinitely large slab of a porous medium with a thickness of L (equal to the regenerator length). The fluid at each side of the slab is maintained at high and low temperatures, respectively, implemented for the PRTA by the hot and cold heat exchangers. The fluid flow oscillates back and forth through the porous slab and transfers heat between both ends and the fluid and solid phase. The energy equation for each phase for a 1-D representation of the regenerator when the axial thermal conduction is accounted for can be written as (Equations 4.11 and 4.12):

Fluid phase:

$$\epsilon(pc_p)_f \frac{\partial T_f}{\partial t} + \epsilon\left(pc_p\right)_f v_p(t) \frac{\partial T_f}{\partial x} = k_f \frac{\partial^2 T_f}{\partial x^2} + h\beta(T_s - T_f) \tag{5.1}$$

Solid phase:

$$(1-\epsilon)(pc_p)_s \frac{\partial T_s}{\partial t} = k_{fs} \frac{\partial^2 T_s}{\partial x^2} + h\beta(T_f - T_s) \tag{5.2}$$

The energy mechanisms are as follows:

- Energy absorbed by the fluid $\epsilon(\rho c_p)_f \frac{\partial T_f}{\partial t}$ and solid $(1-\epsilon)(\rho c_p)_s \frac{\partial T_s}{\partial t}$, respectively, where ρ is the density, c_p the specific heat capacity, ϵ the porosity of the regenerator T the temperature and t the time.
- Energy transferred from the fluid because of motion by $\epsilon(\rho c_p)_f\, v_p \frac{\partial T_f}{\partial t}$, where v_p is the pore fluid flow velocity of the regenerator and x the position in length direction.

- Heat transferred by conduction through the fluid $k_f \frac{\partial^2 T_f}{\partial x^2}$ and solid $k_s \frac{\partial^2 T_s}{\partial x^2}$, respectively, where k is the thermal conductivity.
- Heat transferred by convection to the fluid $h\beta(T_s - T_f)$ and solid $h\beta(T_f - T_s)$ respectively, where h is the heat transfer coefficient and β the interfacial area per unit volume of porous media because the regenerator is treated as a volume made up of void space and solid, therefore, heat transfer is a function of surface area, and porous packed beds are described in terms of wetted surface area per unit volume.

5.1.1 Solution Model

The heat conduction term is assumed to be negligible in the governing equations (Schumann model). This assumption is physically justified based on the small temperature spans being used in the experiments and the small values we expect for the conductivities. Therefore, the equations are as follows:
Fluid phase:

$$\epsilon(pc_p)_f \frac{\partial T_f}{\partial t} + \epsilon\left(pc_p\right)_f v_p(t) \frac{\partial T_f}{\partial x} = h\beta(T_s - T_f) \tag{5.3}$$

Solid phase:

$$(1 - \epsilon)(pc_p)_s \frac{\partial T_s}{\partial t} = h\beta(T_f - T_s) \tag{5.4}$$

For the model a harmonic series analysis is applied to yield the solution [35]. A Fourier series with *2*nd order is assumed and higher harmonics are therefore neglected, this leads to:

$$T(x,t) = T_0(x) + Re\left[T_1(x)e^{j\omega t}\right] \tag{5.5}$$

where *Re*[ ] indicates that the real part of the function is used. For this reason T_1 can be complex which indicates the amplitude and phase. $T_0(x)$

is written as T_0, and $T_1(x)$ as T_1 where it is implied that T_0 and T_1 are functions of position only:

$$T(x,t) = T_0 + Re\left[T_1 e^{j\omega t}\right] \tag{5.6}$$

The temporal and spatial derivative can be expressed by:

$$\frac{\partial T}{\partial t} = \frac{\partial}{\partial t}\left(T_0 + T_1 e^{j\omega t}\right) = j\omega T_1 e^{j\omega t} \tag{5.7}$$

$$\frac{\partial T}{\partial x} = \frac{\partial}{\partial x}\left(T_0 + T_1 e^{j\omega t}\right) = \frac{dT_0}{dx} + \frac{dT_1}{dx} e^{j\omega t} \tag{5.8}$$

In terms of the series expansion approach, the pore fluid flow velocity of the regenerator is rewritten as:

$$v_p(t) = \frac{1}{\epsilon}\frac{A_D}{A_R}\frac{S}{2}\omega \cos(\omega t) = Re\left[u_1 e^{j\omega t}\right] \tag{5.9}$$

with the following definitions:

$$v_p^{max} = \frac{1}{\epsilon}\frac{A_D}{A_R}\frac{S}{2}\omega = L_{sw}\omega = u_1 \tag{5.10}$$

where L_{sw} defines the scaled swept distance. Insert the substituted velocity $v_p(t)$, the assumed solution and the derivatives for T_f and T_s in the governing equation for the fluid leads to:

$$\epsilon\left(pc_p\right)_f j\omega T_{f0} e^{j\omega t} + \epsilon\left(pc_p\right)_f u_1\left(\frac{dT_0}{dx} + \frac{dT_{f1}}{dx} e^{j2\omega t}\right) = h\beta\left(T_{s0} - T_{f0}\right) + h\beta(T_{s1} - T_{f1})e^{j\omega t} \tag{5.11}$$

This equation provides information because linearly independent components must balance each other:

- 0^{th} order: $0 = h\beta(T_{s0} - T_{f0}) \Rightarrow T_{s0} - T_{f0}$, the average temperatures of solid and fluid are the same.

- *2nd* order: $\epsilon(\rho c_p)_f\, u_1 \frac{\partial T_{f1}}{\partial x} e^{j2\omega t} = 0 \Rightarrow \frac{\partial T_{f1}}{\partial x} = 0$, The amplitude of the fluid waveform is independent of position.
- *1st* order leads to the governing equation for the fluid phase:

$$\epsilon\left(pc_p\right)_f j\omega T_{f1} + \epsilon\left(pc_p\right)_f u_1 \frac{dT_{f0}}{dx} = h\beta(T_{s1} - T_{f1}) \qquad (5.12)$$

Inserting the assumed solution and the derivatives for T_f and T_s in the governing equation for the solid phase leads to:

$$(1-\epsilon)\left(pc_p\right)_s j\omega T_{s1} = h\beta(T_{f1} - T_{s1}) \qquad (5.13)$$

The combination of the equation for the fluid and solid phase extracts further information. T_{s1} is a linear function of T_{f1} and both are not a function of position, therefore, the finding of the fluid and solid phase equation is that $\frac{\partial T_{f0}}{\partial x}$ is not a function of position. From this it follows that the average solid and fluid temperature gradient is constant (e.g., linear variation).

Considering the linear temperature gradient through the regenerator, a non-dimensional temperature can be defined as follows:

$$\theta = \frac{T - T_0}{L_{sw}\frac{dT_0}{dx}} \qquad (5.14)$$

where $T - T_0 = T_1$ and so the amplitude of the temperature can be expressed by:

$$T_1 = \theta_1 L_{sw} \frac{dT_0}{dx} \qquad (5.15)$$

Using θ in Equations 5.12 and 5.13 makes the fluid and solid equations non-dimensional: Fluid phase:

$$j\theta_{f1} = \frac{h\beta}{\epsilon\left(\rho c_p\right)_f \omega}(\theta_{s1} - \theta_{f1}) \qquad (5.16)$$

Solid phase:

$$\frac{(1-\epsilon)(pc_p)_s}{\epsilon(pc_p)_f} j\theta_{s1} = \frac{h\beta}{\epsilon(\rho c_p)_f\omega}(\theta_{f1} - \theta_{s1}) \tag{5.17}$$

Two non-dimensional parameters can be found:

$$G = \frac{h\beta}{\epsilon(\rho c_p)_f\omega}, \quad K = \frac{(1-\epsilon)(pc_p)_s}{\epsilon(pc_p)_f} \tag{5.18}$$

The parameter *G* is comparable with a form of *NTU* (Number of Transfer Units) and represents the ratio of the heat transfer between the phases to the fluid thermal capacity. The parameter *K* expresses the entrained thermal mass ratio between the solid and fluid phase. Inserting the parameters *G* and *K* into Equation 5.16 and 5.17 yield the final equations. For the solid phase:

$$\theta_{s1} = \frac{G\theta_{f1}}{G+jK} \tag{5.19}$$

and, out of it, for the fluid phase:

$$\theta_{f1} = \frac{G+jK}{K-jG(K+1)} \tag{5.20}$$

5.2 Determination of the Heat Transfer Coefficient

5.2.1 Model combined with Experiment

The experimental in combination with the analytical model can solve Equation 5.20 and the heat transfer coefficient can be determined. The absolute value of θ_{f1} is therefore calculated with the experimental data by (refer to Equation 5.15):

$$\theta_{f1} = \frac{T_{f1}}{L_{sw}\frac{dT_0}{dx}} \tag{5.21}$$

where T_{f1} is the temperature amplitude of the temperature signals of the regenerator during cyclic equilibrium, $L_{sw} = \frac{1}{\epsilon}\frac{A_D}{A_R}\frac{S}{2}$ is the scaled swept distance and $\frac{dT_0}{dx}$ is the temperature gradient through the regenerator. The parameter K is determined with the physical properties for the regenerator tested. Resultant from Equation 5.20 the parameter G is then computable and the only unknown variable, heat transfer coefficient, is determined by solving Equation 5.18 for the parameter G.

5.2.2 Assumptions and Parameters

The assumptions for the determination of the heat transfer coefficient are summarized below:

- Thermal conduction of the fluid and solid are insignificant.
- Fluid flow effects like mixing or wall channeling is not considered.
- The temperature amplitude throughout the regenerator is the same.
- The temperature gradient throughout the regenerator is linear.
- The heat transfer to the regenerator chamber wall is zero.
- The average temperatures of the solid and fluid are the same.

The following parameters are assumed to be constant (fixed parameters): density and specific heat capacity of the fluid and solid, heat transfer surface area per regenerator volume, porosity, length and cross-sectional area of the regenerator and the cross sectional area of the displacer. In contrast the parameters frequency, stroke, temperature amplitude and temperature gradient are variable.

5.2.3 Extreme Cases Model

Based upon the analytic solution for the fluid temperature amplitude, two extreme values can be identified. A lower limit can be determined by:

$$\theta_{f1} = \frac{G+jK}{K-jG(K+1)}, \bar{h} \rightarrow \infty: |\theta_{f1}| = \frac{1}{K+1} = 0.366 \qquad (5.22)$$

and an upper limit by:

$$\theta_{f1} = \frac{G+jK}{K-jG(K+1)}, \bar{h} \rightarrow 0: |\theta_{f1}| = \frac{K}{K} = 1 \qquad (5.23)$$

The upper limit is therefore caused mathematically and the lower limit is affected by the physical properties for the regenerator.
Such limits need to be accounted for as they represent an upper an lower boundary for experimental data that can be used by the analytical model resulting with a meaningful output.

Chapter 6

Test Apparatus and Experimental Results

6.1 Test Apparatus

This chapter gives an overview of the experimental setup of the Passive Regenerator Test Apparatus (PRTA). All components are discussed in detail. Test results are presented at the end of this chapter.

The design of the Passive Regenerator Test Apparatus (PRTA) aims for reliable control of the volumetric fluid flow and temperature span across the regenerator test section. A simple method for achieving this is chosen: a piston-cylinder type fluid displacer, driven by a variable speed DC motor, forces a controlled volume of fluid back and forth through a closed loop circuit. A crank arm mechanism converts the rotational motion produced by the DC motor into a linear piston motion. This assures sinusoidal waveform over time at a given rotational speed of the motor. The regenerator is situated between two shell and tube heat exchangers (HEX) as shown in Figure 6-1. The heat exchangers are made up of straight aluminum tubes of diameter 1.7 mm and a length of 240 mm. The housing inner diameter of the HEX is 31 mm which is equal to the diameter of the regenerator housing. The porosity of the HEX is estimated to be $\epsilon_{HEX} = 0.25$. The heat exchangers are hooked up to a chiller and heater unit, respectively. The chiller unit has a cooling capacity of 1.2 kW with an operating range between -25 ºC and 80 ºC. The maximum flow rate of the chiller unit is 28 Liters/min. The heater unit is also a chiller with an operating range between -40 ºC and 200 ºC, with maximum heating and flow rate of 0.8 kW and 15 Liters/min, respectively. Both units are operated using distilled water and can thus not be set below the freezing point.

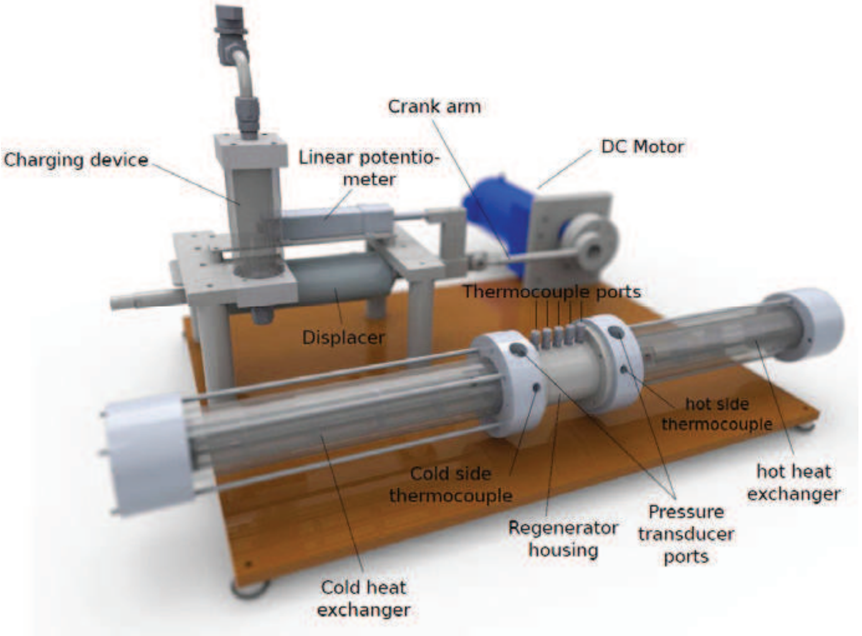

Figure 6-1: Experimental apparatus

A circular tube with diameter d_r = 31.7 mm and length L_r = 71.2 mm made of plastic (Polyixymethylene) is used as regenerator housing and situated between hot and cold HEX as shown in Figure 6-1. The shell can accommodate different regenerator geometries such as wire meshing, packed particles, perforated plates, parallel channels, plates or tubes. At each ends of the regenerator two fine tip, type-E thermocouples (diameter 0.5 mm) are used to measure temperature. The response time of these thermocouples is on the order of 10 ms and much smaller than the actual physical cycle time. Five additional thermocouples can be placed at equidistant axial positions inside the regenerator. Their radial position depends on the regenerator geometry to be tested. An additional two thermocouples can be placed between the two heat exchangers and the displacer to measure temperature difference across the heat exchangers. A potentiometer is placed on top of the displacer to resolve displacer position as a function of time. The pressure drop across the regenerator can be measured with the two pressure transducers at each end of the regenerator. In addition, another pressure transducer is placed between the HHEX and the displacer to measure pressure drop across the HHEX. A schematic representation of the PRTA is shown in Figure 6-2. All measured quantities (in total 11 temperature, 3 pressure and 1 potentiometer readings) are also shown in Figure 6-2.

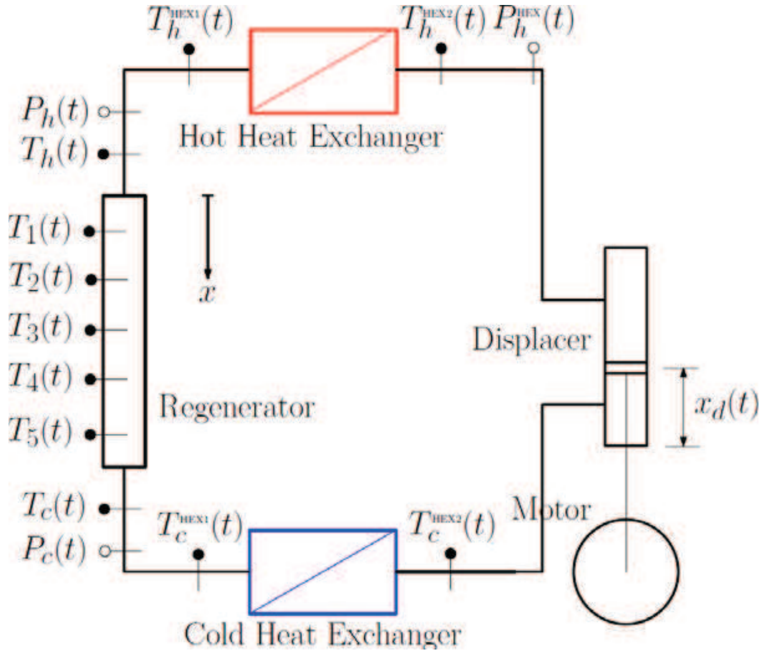

Figure 6-2: Schematic of PRTA

6.2 Test Section

The present work deals with two regenerator geometries: a microchannel regenerator and a packed particle bed regenerator made of spherical particles. The microchannel regenerator is made up of three bronze pucks (see Figure 6-3) and was produced using laser sintering technology at the University of Salerno in Italy.

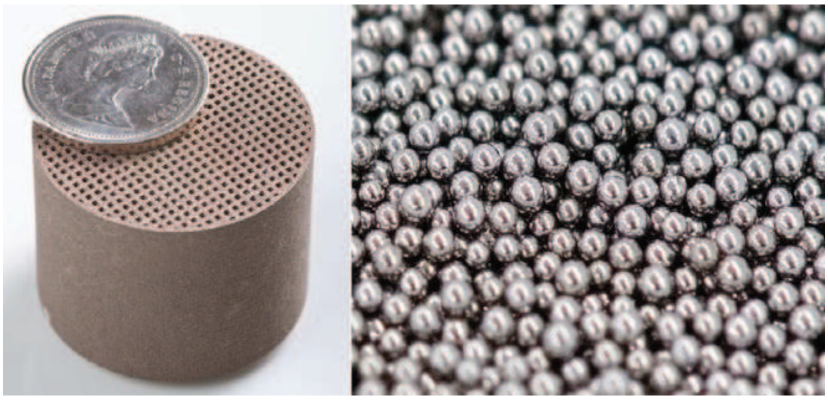

Figure 6-3: Photograph of a sintered micro channel puck and spheres

The channel height is h_c = 0.7 mm and the wall thickness h_w = 0.5 mm resulting in a hydraulic diameter equal to the channel height $d_h = h_c$. The surface finish is fairly rough and is estimated to be one order of magnitude smaller than the hydraulic diameter. The porosity is ϵ= 0.32.

Table 6-1: Regenerator matrix geometrical properties

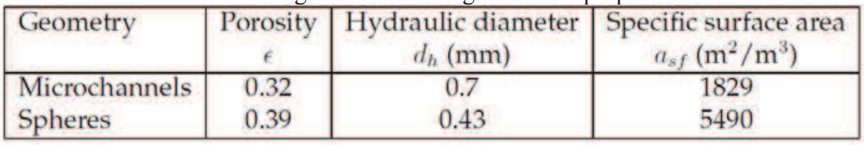

Geometry	Porosity ϵ	Hydraulic diameter d_h (mm)	Specific surface area a_{sf} (m^2/m^3)
Microchannels	0.32	0.7	1829
Spheres	0.39	0.43	5490

The stainless steel spheres have a diameter of d_p = 1mm. The porosity of the spheres is determined by measuring the mass of the spheres after it is packed in the regenerator. The porosity, hydraulic diameter and the specific interfacial surface area are compared in Table 6-1. It can be seen that the porosity of the two regenerators is slightly different. The hydraulic diameters are in the same order of magnitude. However the specific surface area of the spheres is about three times as large compared to the microchannels.

The regenerators also differ in terms of thermal properties. They are summarized in Table 6-4.

Table 6-2: Regenerator matrix thermal properties

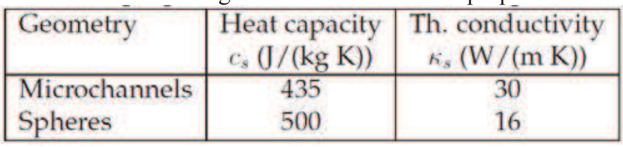

Geometry	Heat capacity c_s (J/(kg K))	Th. conductivity κ_s (W/(m K))
Microchannels	435	30
Spheres	500	16

While the heat capacities of the two regenerators are similar, this is not the case for the thermal conductivity. Bronze shows a larger thermal conductivity (by a factor of two) than stainless steel. It must be noted that these are intrinsic values and not effective values. Due to the sporadic contact of the spheres it can be expected that the geometrically effective thermal conductivity of the spheres is even smaller than its intrinsic value. The microchannel geometry is well suited for both experimental and theoretical determination of heat transfer and pressure drop characteristics. The homogeneity in the axial direction and the rectangular front face makes this type of regenerator a well suited candidate for numerical simulation of heat transfer and pressure drop characteristics that can be validated against experimental results.

6.3 Experimental Procedure

There are three degrees of freedom that can be controlled by the experimentalist:

1. The stroke, L_s, controls the amount of fluid that is displaced during one cycle. The stroke can be adjusted by changing the length of the crank armor the size of the displacer.
2. The frequency determines the duration of the cycle and can be controlled by the voltage supplied to the DC Motor.
3. The time averaged temperature span $T = T_{c0} - T_{h0}$ can be imposed by changing the chiller and heater settings.

In general each experiment is characterized by stroke, frequency and time averaged temperature span. Once the system is in cyclic steady state a number of cycles are recorded. Each signal (temperatures, pressure and displacement from potentiometer) is written in form of a discrete time series to a file. The experiment is repeated using an incremental change in frequency. It is not necessary to maintain the temperature span at a constant value; however, a large temperature span is desirable since it increases the accuracy to measure temperature oscillations (large temperature spans will result in larger temperature oscillations). The thermal oscillations are of particular interest for the extraction of heat transfer data. This procedure is repeated for different stroke values.

Table 6-3: Operating range of PRTA

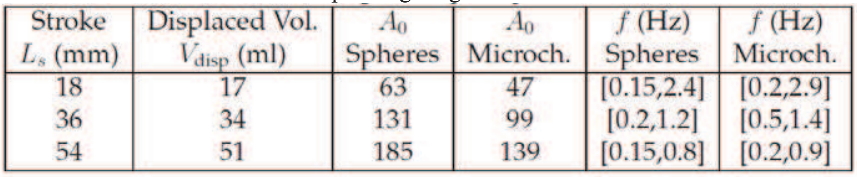

Stroke L_s (mm)	Displaced Vol. V_{disp} (ml)	A_0 Spheres	A_0 Microch.	f (Hz) Spheres	f (Hz) Microch.
18	17	63	47	[0.15,2.4]	[0.2,2.9]
36	34	131	99	[0.2,1.2]	[0.5,1.4]
54	51	185	139	[0.15,0.8]	[0.2,0.9]

Table 6-3 shows the operating range of the PRTA. The maximum operating frequency decreases with increasing stroke because the friction of the piston against the cylinder wall increases. In addition the increased pressure drop of the spheres at higher frequency also limits the maximum frequency.

6.4 Data Processing

The data is processed using a discrete Fourier transform (DFT). Rectangular windows are applied matching beginning and end of the signal to assure sharp spectral resolution. The spectral breakdown of the displacement signal and the reconstructed signal from the spectra is shown in Figure 6-4. It is clearly observable that the piston motion is well approximated by a pure sinusoid with frequency $f = 1.4$ Hz and negligible higher harmonic content.

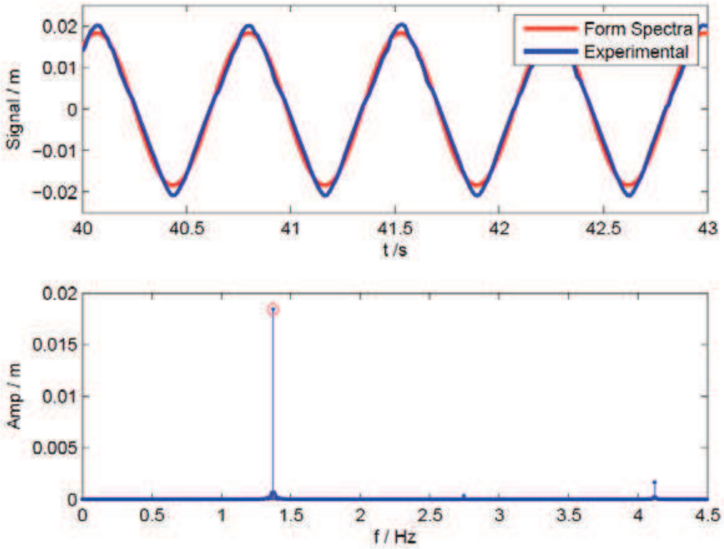

Figure 6-4: Spectra of displacement signal

The spectra for hot side temperature for microchannels and spheres is shown in Figure 6-5 and Figure 6-6, respectively. The temperature reading in the microchannel experiment is well approximated by a pure sinusoid. The temperature reading using the spheres geometry shows significant higher harmonic content. The observation of multiple frequencies is a consequence of the time dependency of transport properties (such as dispersion) or general non linearities (temperature dependency of viscosity). Also spheres induce about one order of magnitude larger pressure drop, causing larger unbalanced torques to the displacer drive. Interestingly the higher order frequencies are a multiple of the dominant frequency. The spectra of the hot side reading in Figure 6-6 has a dominant frequency of $f_1 \approx 0.8$ Hz, the second frequency $f_2 \approx 1.6$ Hz and the third $f_3 \approx 2.4$ Hz.

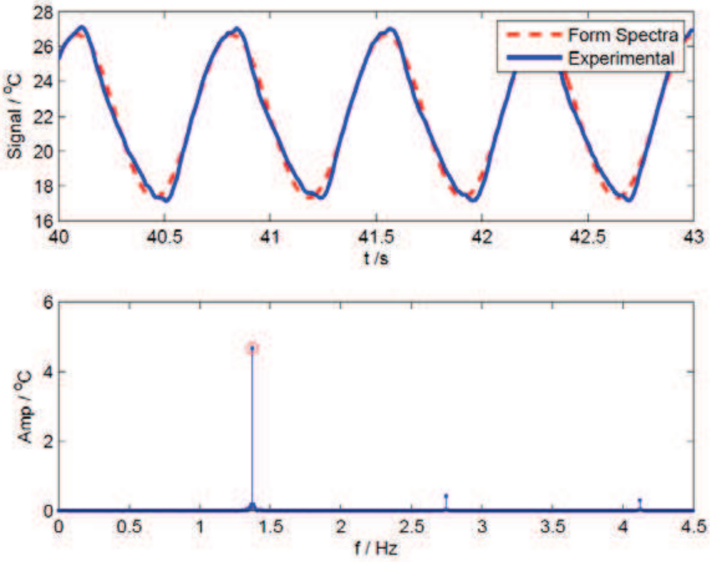

Figure 6-5: Spectra of hot side temperature signal using microchannels

The spectra of the pressure drop signal $p = p_c(t) - p_h(t)$ is shown in Figure 6-7. The pressure drop through the microchannel regenerator is expected to be small, resulting in a rather noisy measurement of the pressure drop signal. Also this signal shows higher harmonic content. It must be emphasized that the theory presented in earlier chapters only applies to the dominant oscillations of all signals, therefore, in what follows, higher order harmonics are neglected. Each experiment consists of 15 time series (temperature, pressure and linear pot signals) resulting in roughly 700 time series for all experiments conducted.

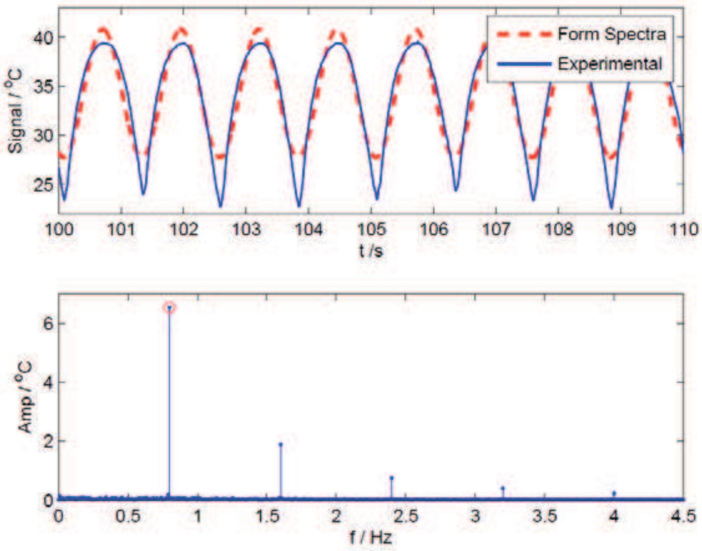

Figure 6-6: Spectra of hot side temperature signal using spheres

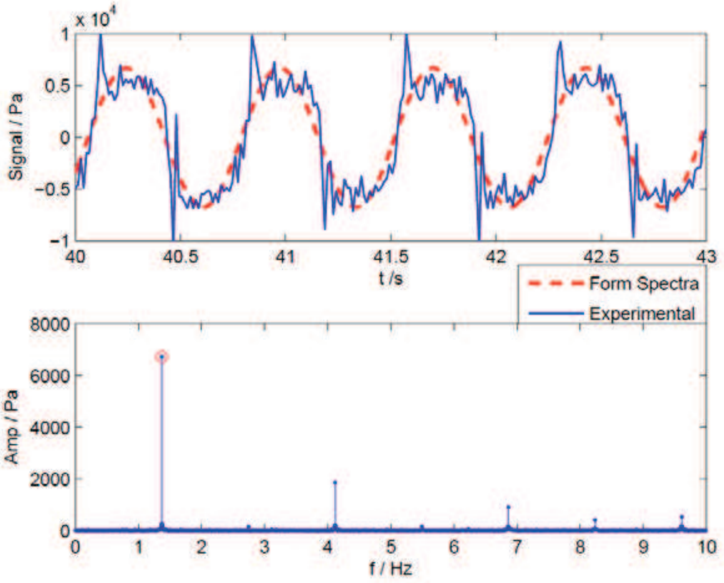

Figure 6-7: Spectra of pressure drop for a microchannel experiment

6.5 Experimental Results

The experimental results of temperature and pressure readings are presented over the entire frequency and stroke range that is covered experimentally. First, the time averaged temperature span for both geometries is considered. Figure (8.8) shows the mean temperature difference between hot and cold side for all strokes and frequencies recorded.

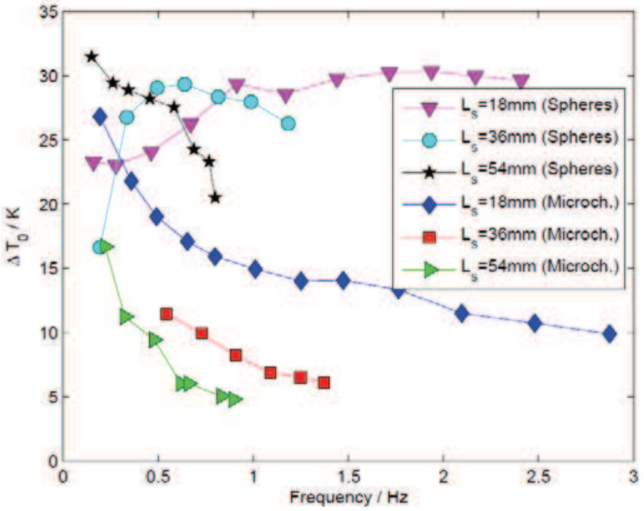

Figure 6-8: Time averaged temperature difference between hot and cold side for both geometries.

The microchannels show reduced temperature spans as the frequency is increased mainly due to heat transfer limitations in both heat exchanger and regenerator as the frequency increases. The temperature span also consistently drops as the stroke is increased. A higher stroke will increase the velocity in the regenerator and thus limit the heat transfer. The situation for the corresponding experiment using spheres shows the reverse effect at small frequencies. For strokes L_s = {18, 36}mm the temperature span increases first with frequency until it reaches a maximum value and drops again. At the highest stroke the temperature span is maximal in the low frequency limit and decreases monotonically with frequency. It is suspected that at low frequency other heat transfer effects lower the regeneration process. Dispersion is known to be significant at low frequency for a packed particle bed geometry [25] and might be responsible for significant diffusion in the regenerator. As the frequency increases and stroke increases advection is expected to be amplified such that diffusion effects become negligible. This would explain the monotonically dropping temperature span for the largest stroke L_s = 54mm.

In general the temperature spans using spheres are larger than corresponding spans for the microchannels at the same chiller sink and heater source temperature. This indicates that the spheres act as a more effective regenerator.

The temperature amplitudes for the micro channel and sphere geometry are shown in Figure 6-9 and Figure 6-10, respectively. In general the cold side amplitudes are slightly larger than the hot side amplitudes. The amplitudes at stroke Ls = 18 mm remain fairly constant over frequency but are largest at intermediate frequencies. Again, this might be an indicator for transport modes like dispersion that are pronounced at low frequencies. At higher strokes, amplitudes drop with increasing frequency. The amplitudes are a function of both the heat transfer quality and the temperature span (because there can not be thermal oscillation without the presence of a temperature difference between hot and cold end). Therefore the decreasing amplitudes at higher frequencies can be understood as an indicator for increased heat transfer. It is interesting to note that the intermediate stroke value shows higher amplitudes (in the corresponding frequency range) than the highest stroke amplitudes.

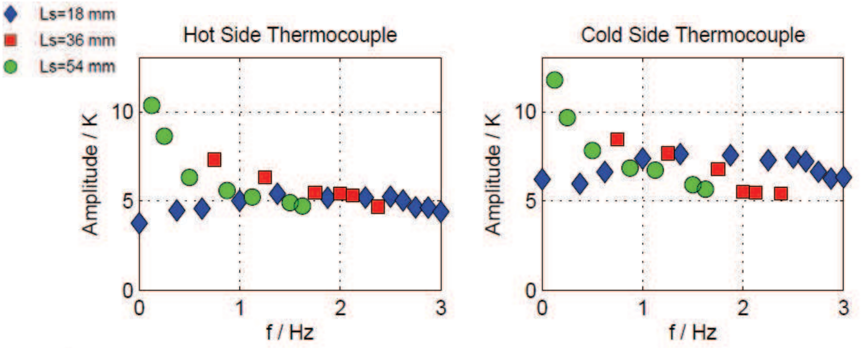

Figure 6-9: Temperature amplitude for microchannel experiments.

A similar behavior can be observed for the sphere experiment. The difference is that the amplitudes are in general smaller at higher frequencies compared to the microchannel experiment. This behavior it to be expected as the packed spheres should allow a better heat transfer.

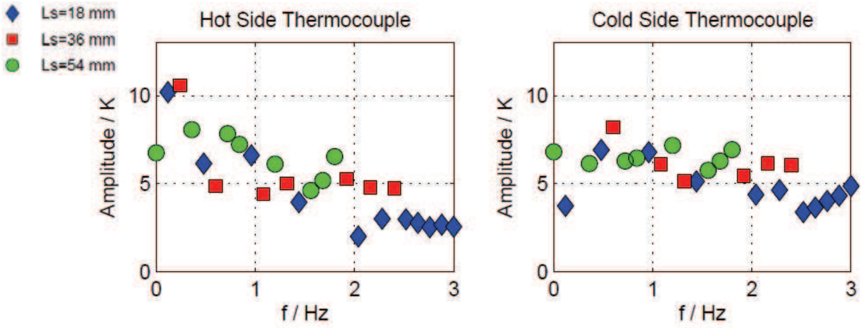

Figure 6-10: Temperature amplitude for packed particle bed experiments.

The pressure drops across the heat exchanger, the microchannel regenerator and the spheres regenerator are shown in Figure 6-11. All pressure drop magnitudes increase with frequency and stroke (as a result of increased fluid velocities). As expected, the spheres show the largest pressure drop. The heat exchangers show the lowest pressure drop because of the low porosity, and it is in the same order of the heat microchannel structure.

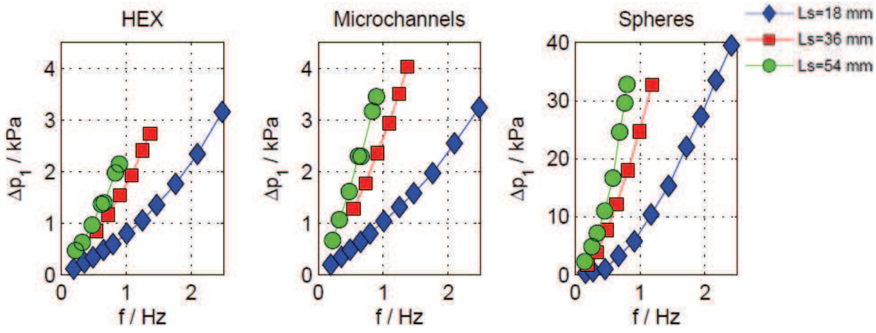

Figure 6-11: Pressure drop of heat exchanger, microchannels and spheres geometry.

6.6 The microchannel regenerator and the internal axial temperature gradient

Heat transfer in a parallel plate type of design is largely limited by the laminar nature of the fluid flow. Therefore, in order to obtain a satisfactory heat transfer the boundary layer needs to fill as much as possible the cross sectional area of the gap between the plates. For typical flow rates in magnetic refrigerators smooth parallel plate design performs poorly if the gap is larger than 0.1 mm. If the refrigerator operates at high frequencies (4-5 Hz per regenerator) the gap needs to be substantially smaller (0.02-0.05 mm). It is a technological challenge prototyping regenerators with such small features while ensuring a consistent hydraulic diameter. Alternative matrix patterns could match the performance with significantly larger geometrical features. For instance Figure 6-12 compares the temperature distribution in the gap between parallel plates and in a squared straight channel which sides are of the same size of the gap between the plates. For the same gap size and porosity, the micro-channel option offers 70% more surface contact, and a larger boundary layer due to the more convoluted geometry.

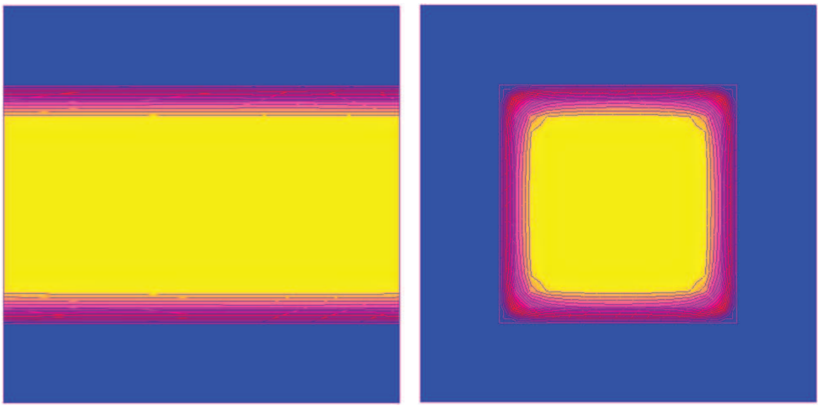

Figure 6-12: Parallel plate and square channel compared: fluid temperature distribution.

We were looking for a simple and effective way of producing a non-particle based passive regenerator matrix. The technology needed to generate a geometrical pattern consistently and cheaply, and to be compatible with a suitable regenerator material. The Mechanical Engineering Department at the Universita' di Salerno, Italy, made available a laser sintering unit set up for bronze rapid prototyping. Although this technology does not quite produce features as small as specified (>0.2 mm), it exceeded the specifications for all other requirements. It also created parts with relatively coarse surface finish (0.05 mm), which is desirable for increasing the surface contact and for inducing flow turbulence. In addition, bronze has adequate thermodynamic properties as a passive regenerator material, offering a relatively large density, heat conduction coefficient, and specific heat. In addition it does not react with water, which is used as heat transfer fluid.

The chosen geometry was based on a pattern of squared channels 0.7 x 0.7 mm equally spaced with a wall thickness of 0.5 mm. The channel size was chosen based the smallest diameter recommendable for removing the loose powder particles left in the gaps in the final stage of the manufacturing process, while the wall thickness was chosen for ensuring 30-35 % porosity. The choice of the porosity was based on the fact that spheres typically pact to 36% porosity so a direct comparison could be made. The regenerator resulted in a porosity of 32% when including the peripheral wall. In addition, regenerators were manufactured in 23.5 mm length pucks, which is one third of the cavity depth available in the apparatus regenerator shell. Short pucks are desirable for a number of factors: easier and more accurate manufacturability, ease of powder removal from the micro-channels, modularity in the experimentation, while intentionally breaking down axial thermal losses (point contact conduction between pucks). The following table summarizes the properties of each regenerator puck.

Table 6-4. Regenerator Properties

Specification	**Value**	**unit**
Regenerator Diameter	31.75	mm
Regenerator puck length	23.5	mm
Channel cross section	squared	
Channel cross section side	0.7	mm
Number of channels per puck	732	
Wall thickness	0.5	mm
Regenerator porosity	32%	
Regenerator mass	100	g
Channel cross section	squared	
Regenerator material	DirectMetal 20 (bronze)	

6.6.1 The instrumentation

In order to measure the fluid temperature in one of the micro-channels a Fiber Bragg Grating (FBG) was implemented with 5 gratings equally spaced at 16.75 mm for an overall span of 67 mm. Therefore the first and last gratings are located approximately 2 mm inside from the respective regenerator end. The layout is showed in the following Figure 6-13.

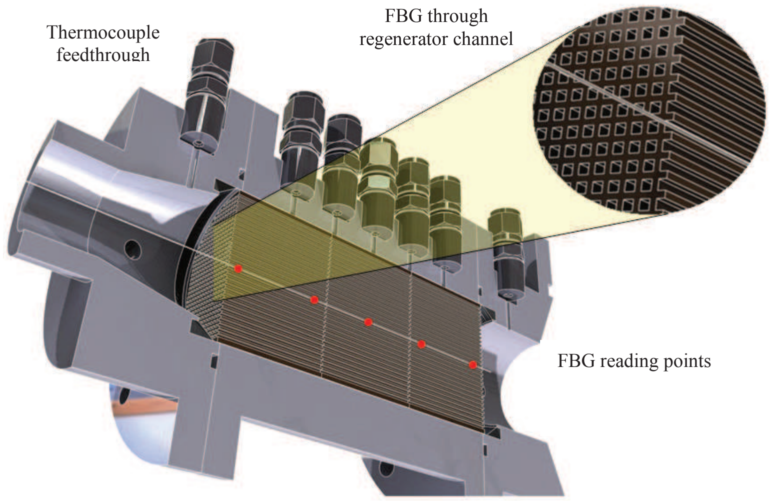

Figure 6-13: Laser sintered micro-channel regenerator, assembly with encasing shell, FBG and transducer location. The figure represents the current experimental set up with three regenerator pucks installed

Fiber Bragg Grating Implementation

Fiber Bragg Grating is a segment of fiber optic reflecting back to the source a specific wavelength of emitted light while still transmitting the rest of the spectrum. This is obtained by locally changing the refractive index at specific intervals (grating). The reflected wavelength is obtained from the following:

$$\lambda_B = 2\,n_{eff}\Lambda \tag{6.1}$$

Where λ_B is the center of the reflected wavelength, n_{eff} is the effective modal refractive index, and Λ is the period of the Bragg grating (Figure 4a). Therefore strain due to a mechanical or thermal stress affects the length of the fiber and thus the period (pitch) Λ. This can be used to monitor temperature or mechanical stress by observing the reflected wavelength shift:

$$\frac{\Delta\lambda_B}{\lambda_B} = (1 - p_\varepsilon)\epsilon + (\alpha_\Lambda + \alpha_n)\Delta T \tag{6.2}$$

Where p_ε is the strain optic coefficient, α_Λ the thermal expansion coefficient, and α_n the thermo-optic coefficient [37].

FBG are a convenient temperature measurement tool for our specific task because it allows multi-point readings along a single fiber (this can be achieved by applying multiple gratings tailored for different wavelengths, Figure 6-14), which can be installed along a single regenerator channel. FBGs reading are averaged over 50 ms (which is in the same order of magnitude of the thermocouple response time or better), to mitigate the signal noise, and they have an accuracy of 0.1 °C, matching or exceeding the specifications of the type E thermocouples used in the same apparatus. In addition, since the fiber occupies only 4% of the channel cross sectional area, it is expected to add a negligible perturbation to the fluid flow field.

Equation (6.1) shows that applying an axial mechanical stress on the fiber would skew the temperature measurement; therefore it was necessary to install the FBG with minimal mechanical constraints. However leaving the fiber unrestricted in the channel could become an issue when immersed in an oscillating fluid flow: it could potentially induce measurement fluctuation, caused by fiber motion, sufficiently large to overcome the useful signal. It was found that the friction against the channel wall was sufficient to maintain the fiber stationary, without adding tensile stress to it.

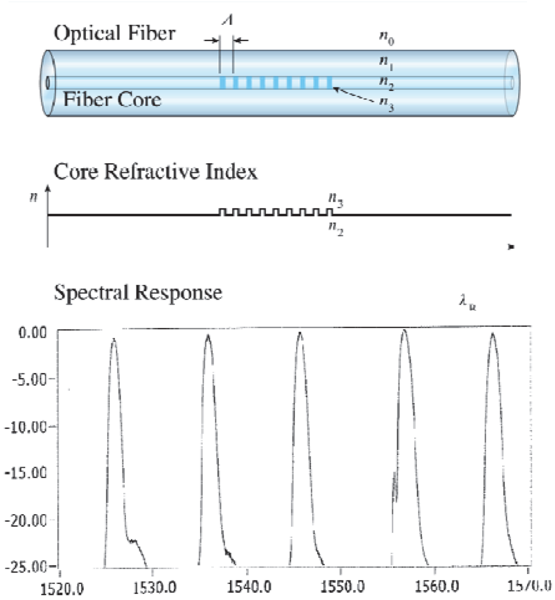

Figure 6-14: (a) FBG wavelength filtering mechanism (wiki) and (b) PRTA fiber reflection spectrum (5-point measurement).

Once the FBG was installed it was necessary to perform a calibration to find the experimental relationship between the wavelength shift and the temperature variation. This was done by setting a constant temperature across the regenerator and obtaining the λ_B for each of the five points for a range of temperatures between 30 and 50 °C. As expected a linear relation was found, reports the Figure 6-15 calibration for the first of the gratings. A similar relation was found for each of the points.

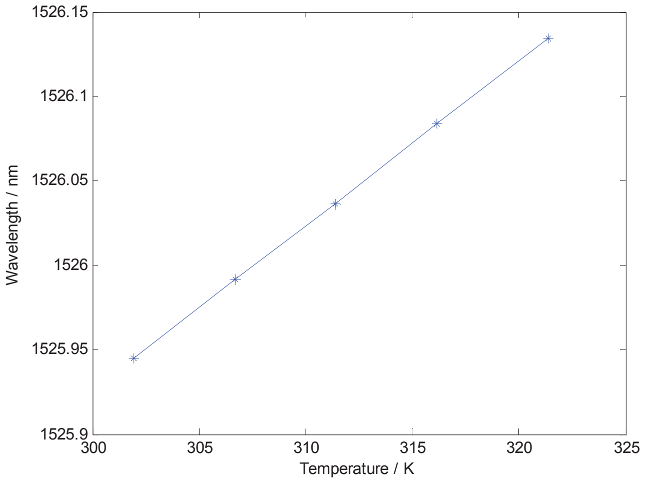

Figure 6-15: Example of calibration curve for first grating wavelength reflection response as function of temperature only.

The Fiber Bragg Gratings produced a clean usable signal once averaged over 50 samples while operating at 1 kHz sampling rate.

Figure 6-16a illustrates a strip chart of the temperatures at each grating and

Figure 6-16b shows the temperature distribution across the channel. A typical trend shows a reasonably constant gradient along the central part regenerator and slightly larger gradients toward the ends. Amplitudes also were larger at the ends rather than in the central region. It is to be noted that the upper and lower bound represent in the

Figure 6-16b are over a cycle and therefore might not be simultaneous in real time observations. Steeper gradients and larger amplitudes at the inlet flow of the regenerator were to be expected as this is the region where the temperature of the solid is more largely affected by the fluid. The temperature spans obtained could not exceed 15 K because the heat exchanger proved to be quite ineffective in constraining the cold temperature side given the large enthalpy flux. The challenge was most obvious at higher Reynolds Numbers where the cold side could easily settle at temperatures 15 to 20 K above the heat exchanger outer loop temperature. A regenerator matrix offering a larger heat transfer, such as smaller spheres or microchannels with larger surface area (smaller hydraulic diameter, smaller webbing to maintain the porosity constant), would allow to maintain a larger temperature gradient between the hot and cold source.

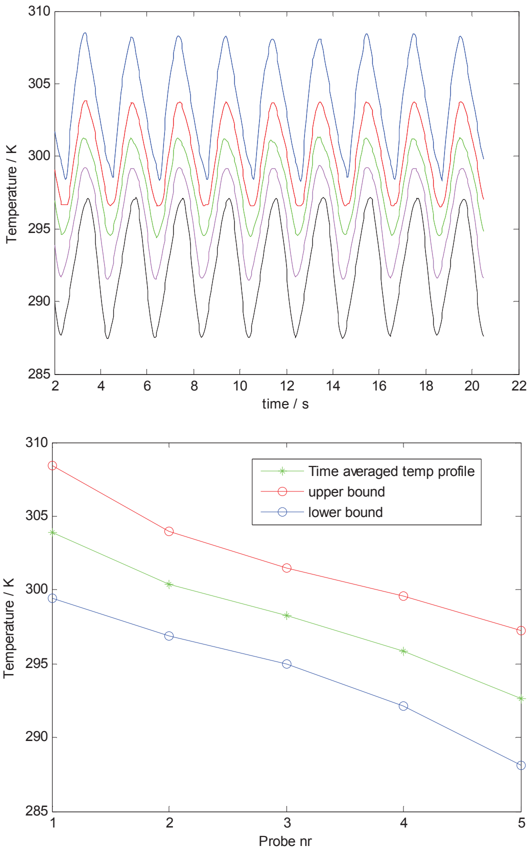

Figure 6-16: FBG temperature reading along regenerator channel. AStrip chart of the raw data and time averaged temperature profile showing the upper bound and lower bound.

Chapter 7

Experimental Evaluation

7.1 Friction Factor

The friction factor for the microchannel regenerator is sow in Figure 7-1. In general, finite element model overestimates the pressure drop of the microchannel regenerator. However, the FE calculation captures the general trend with an acceptable error with respect to experimental data.

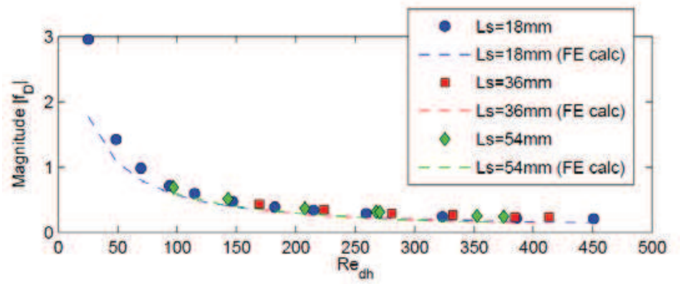

Figure 7-1: Microchannel friction factor

The friction factor of the spheres geometry at T = 20 ºC is shown in figure Figure 7-2. The experimental data is compared against the Ergun correlation [36]. It must be noted that the RMS value of the Ergun correlation is shown in figure (10.2) because Ergun tested spheres only in steady flow experiments. The Ergun correlation matches the experimental data well in the low Reynolds number regime. At higher Reynolds numbers the Ergun correlation underestimates the experimental data. This and the influence of a non-isothermal condition on the friction factor must be further investigated.

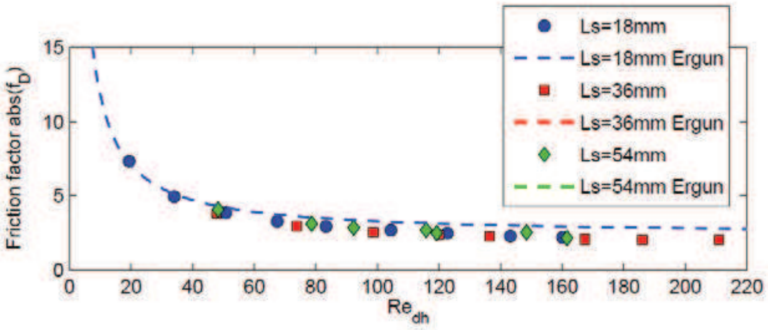

Figure 7-2: Friction factor of sphere geometry

It must be noted that the pressure signals are very noisy especially when components with small pressure drops are measured. Still, the friction factors agree with the experimental data within an acceptable limit. However, the goal of this section is not to find a perfect model that accurately reproduces the experimental data. The models are used to check whether the experimental data is sufficiently close to widely used correlations and models based on first principles and indicates that the test apparatus qualitatively operates as expected.

7.2 Nusselt Number

The methodology illustrated in Chapter 5 for *Nu* extraction from the experimental data is implemented for the microchannel structure and spheres. The methodology basically quantifies the fact that temperature gradient and inlet/outlet temperature amplitudes are correlated by the heat transfer quality. The results are presented in this section.

Figure 7-3 illustrates the *Nu* for microchannels for strokes of 2, 4, and 6 cm. The Reynold Number (Re_{dh}) ranges between 20 and 450 depending on the stroke/frequency used for the test. Flow is laminar for the full range. The tests show a weak dependence on the Re_{dh} with *Nu* ranging from 0.5 to 3.5.

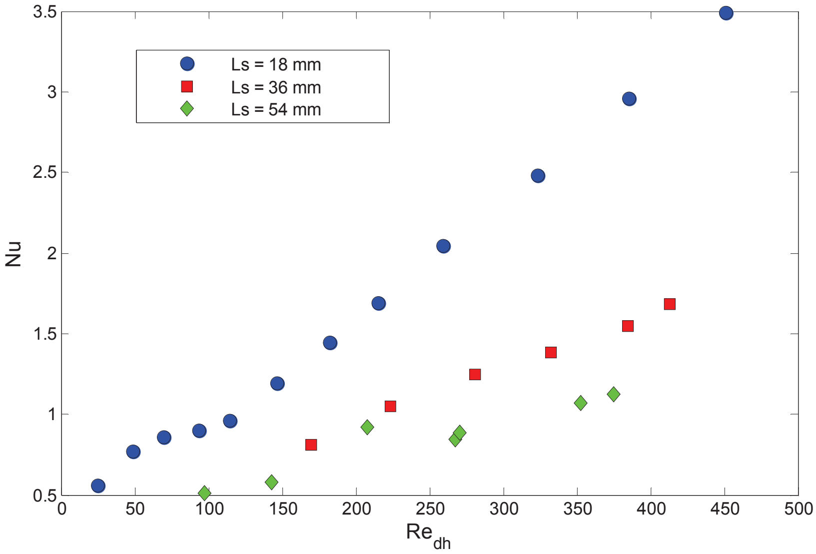

Figure 7-3: Experimentally obtained Nusselt numbers for microchannel geometry

The results are in a reasonably good agreement with literature data reporting $Nu = 3.6$ for square channels at uniform temperature and fully developed flow [38]. The dependency on Re_{dh} is expected to be caused by the fact that the microchannel regenerator is relatively short (approximately 6.5 cm) and therefore the fully developed flow might not strictly apply. This can be observed (Figure 7-4), where Nu is evaluated [39] as function of Re_{dh} if fully developed flow cannot be assumed. The plot was derived using the Muzychka formulation of Nu for thermal developing laminar flow in a square duct. A similar dependency to the experimental values is observed, however the values, even if in the same order of magnitude are 50% to 100% larger. The feel that it has been developed so far with the Nu extraction via this new methodology is that higher performance regenerators are required for more accurate estimates. After all such poor regenerators have no purpose in a practical application. The reason why they were used in this analysis was availability, and cross-referencing with available literature.

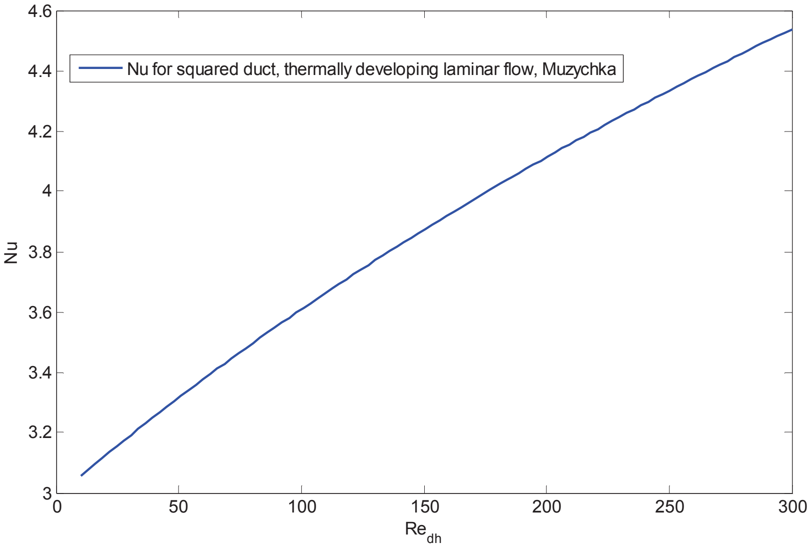

Figure 7-4: Nu as function of Re_{dh} for square channels

The Nusselt number for the spheres geometry is shown in Figure 7-5. It can be seen that the Nusselt number increases faster with frequency than the Nusselt number of themicrochannels does. However, large scattering of the data is observable in the low frequency limit where the data density is high. It is well known that the Nusselt number scatters in the low frequency limit because other effects than advection are pronounced that are not modeled. Recently, Engelbrecht [28] defined new a correlation function for the Nusselt number of a packed bed. The correlation results from a single blow type experiment using water as working fluid. However, the size of the test section is very similar to the experimental setup presented in this work. The correlation is given by

$$Nu = 0.7Pr^{0.23}Re^{0.6} \tag{7.1}$$

Where the Reynolds number is based on hydraulic diameter and the superficial velocity, i.e. $Re = \epsilon Re_{dh}$.

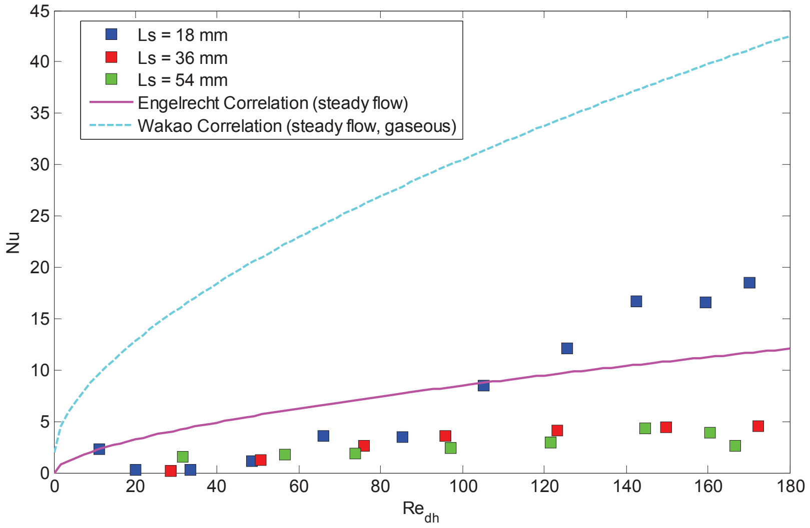

Figure 7-5: Experimental Nusselt numbers versus Engelbrechts and Wakao correlation for spheres.

Figure 7-5 shows Engelbrechts correlation and the experimentally obtained Nusselt numbers as a function of Re_{dh}. The Nusselt numbers obtained at high strokes are lower than predicted by Engelbrechts correlation. At low stroke and high frequency the experimentally obtained Nusselt numbers are higher than predicted by Englebrechts correlation. Since Engelbrechts correlation corresponds to a single blow type experiment only the RMS value is shown. More data needs to be taken in the low frequency range and processed with extended models to understand low to medium frequency behavior. It must be noted, that the tests include low frequency data sets that are rather not relevant for the operation of a regenerator in an actual device. Overall still the Englebrechts and experimental values are in the same order of magnitude.

Figure 7-5 also compares the results to the Wakao [24] predictions. This case clearly shows how the existing literature for single blow using gas as heat transfer fluid could significantly over predict, based on a physical phenomenon that deviates substantially from the system we are trying to characterize (oscillating liquid). Such observation underlines the fact that this area of study needs further investigation.

Finally the Nusselt numbers of the two geometries are shown in Figure 7-6. It can be seen that over the entire frequency range the sphere geometry shows generally a higher Nusselt number than the microchannel geometry. This can be expected due to the large specific surface area of the particle bed geometry. The larger sensitivity of the packed spheres to the frequency (and Reynold number) is due to the more pronounced tortuosity of the fluid path. This induces a more "turbulent-like" fluid flow and therefore the heat transfer is more largely affected by the fluid velocity.

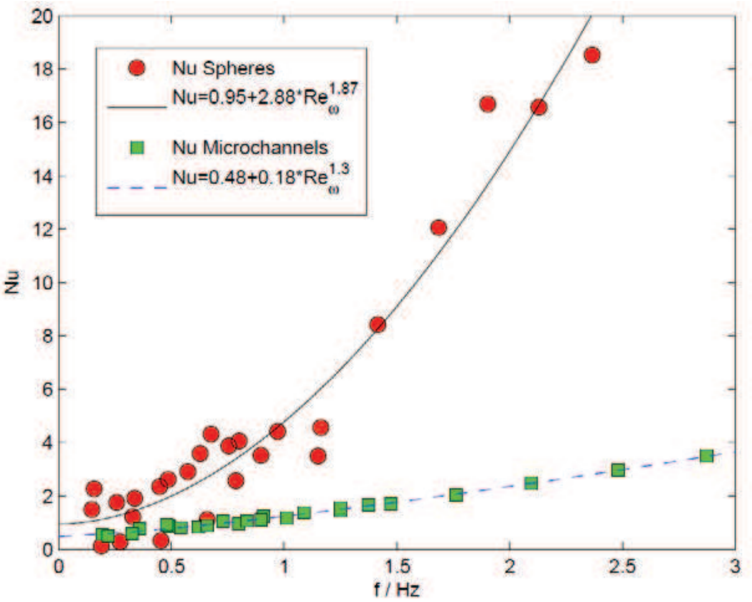

Figure 7-6: Comparison of Nusselt numbers of the two geometries.

Chapter 8

Conclusions and Recommendations

This thesis focuses on the thermohydraulic properties of oscillating flow in porous media. A theoretical method is presented to extract friction factor and Nusselt number. Results are compared to available literature. A test apparatus is presented used to test various regenerator geometries. The goal of this research is to develop a clear theoretical and experimental procedure that determines friction factor and Nusselt number for various types of regenerators.

In the first part of this thesis, models for momentum and energy conservation are presented that hold on a macroscopic scale using a harmonic approximation technique. Such methodology allows extracting the *Nu* by only knowing the mean temperatures and the fluctuations at the ends of the regenerator and the fluid velocity. In the second part of this thesis an experimental device is described and raw experimental data is presented. Also, a fiber Bragg sensing system was rigged up to measure the fluid temperature along one regenerator channel. This allowed verifying if, in the experimental parameter space of interest, assuming a close-to-linear temperature gradient was reasonable.

The result analysis concluded the following. The friction factors obtained from experiments show fair agreement with model predictions. The Nusselt number for the spheres geometry, compared against a correlation obtained from a steady flow experiment and shows a discrepancy at low frequency. The Nusselt numbers for the microchannel geometry was evaluated to be in the range of existing literature, with the tendency at underestimating its value in the low Reynolds number/ frequency range. This is caused by limitations of the experimental apparatus.

Recommendations for future work are the following. First step is to test and analyze regenerators with higher effectiveness. Much of the uncertainty in the results is caused by choosing regenerators with poor performance (low Heat transfer Units). In the real world a choice of spheres in the 300-600 μm would be more appropriate. The next step would be the development of a passive apparatus using a unidirectional flow path in the heat exchangers, while maintaining an oscillating flow in the regenerator. This could be achieved with the use of a pump and a hydraulic circuit controlled by proportioning electromagnetic valves. Such an apparatus would allow operating at higher frequencies with reduced noise and inertial effects due to oscillating flow in as system with relatively large hydraulic diameters.

References

[1] Rowe, A., Tura A., Dikeos J., Chahine R, “Near Room Temperature Magnetic Refrigeration”, *Proceedings of the International Green Energy Conference,* 12-16 June 2005, Waterloo, Ontario, Canada.

[2] Gschneidner, K.A., and Pecharsky, V.K., *Intermetallic Compounds:* Vol. 3, *Principles and Practise.* John Wiley, pp. 519, 2002.

[3] Rowe, A., “Active Magnetic Regenerators: Performance in the Vicinity of Para-Ferromagnetic Second Order Phase Transition” Ph.D. Thesis, University of Victoria, Victoria 2002.

[4] Yu, B.F., Gao, Q., Zhang, B., Meng, X.Z., Chen, Z., “ Review on Research of Room Temperature Magnetic Refrigeration” *International Journal of Refrigeration,* vol. 26, pp 622-636, 2003.

[5] Green, G., Chafe, J., Stevens, J., Humphrey, J., “ A Gadolinium-Terbium Active Magnetic Regenerator” in *Advances in Cryogenic Engineering*, vol.35, pp. 1165, 1990.

[6] Zimm, C., Johnson, J., Murphy, R.W., “Test Results on a 50 K Magnetic Refrigerator” in *Advances in Cryogenic Engineering*, vol. 41, pp 1675, 1996.

[7] Zimm, C., Jastrab, A., Sternberg, A., Pecharsky, V., Gschneidner, K., Osborne, M., Anderson, I., “Description and Performance of a Near-Room Temperature Magnetic Refrigerator” in *Advances in Cryogenic Engineering*, vol. 43, pp. 1759, 1998.

[8] Coulumb, D. “The IIR and the Environmental Challenges Facing the Refrigeration Sector” *Proceedings of IIR International Conference on Magnetic Refrigeration at Room Temperature*, Opening Session, Portoroz, Slovenia, April 11-13 2007, pp 3-5.

[9] K.A. Gschneidner Jr. and V.K. Pecharsky, “Thirty years of near room temperature magnetic cooling: Where we are today and future prospects”, *International Journal of Refrigeration,* vol. 31, pp 945-961, 2008.

[10] Hirano, N., Nagaya, S., Okamura, T., Kawanami, T, Wanda, H., “Development of Room Temperature Refrigerator –Overall Plan-” *Proceedings of IIR International Conference on Magnetic Refrigeration at Room Temperature*, Portoroz, Slovenia, April 11-13 2007, pp 281-287.

[11] Hirano, N., S. Nagaya, M. Takahashi, T. Kuriyama, K. Ito, and S. Nomura, 2002, “Development of Magnetic Refrigerator for Room Temperature Application” in *Advances in Cryogenic Engineeering* volume 47 pp1027-1034.

[12] Zimm, C., Auringer, J., Boeder, A.Chell, J., Russek, S., Sternberg, A., “Design and Initial Performance of a Magnetic Refrigerator with a Rotary Permanent Magnet” *Proceedings of IIR International Conference on Magnetic Refrigeration at Room Temperature*, Portoroz, Slovenia, April 11-13 2007, pp 341-347.

[13] Rowe, A., Tura, A., Richard, M-A., Chahine, R. and Barclay, J., “An Overview of Operating Experience Using the AMR Test Apparatus” in *Advances in Cryogenic Engineering* 49B, pp. 1721-1728, 2004.

[14] Gschneidner, K.A., and Pecharsky, V.K., Tsokol, A. O., “Recent Developments in Magnetocaloric Materials” *Rep. Prog. Phys.* 68 1479-1539, 2005.

[15] Richard, M.A., Rowe, A., Chahine, R., “Magnetic Refrigeration: Single and Multimaterial Active Magnetic Regenerator Experiments”, *J. Appl. Phys.* 95, 2146, 2004

[16] Gschneidner, K.A., and Pecharsky, V.K., Ames Laboratory, Iowa State University, Ames, *private communication*, October 2005.

[17] Hall, J.L., Reid, C.E., Spearing, I.G., and Barclay, J.A., "Thermodynamic Considerations for the Design of Active Magnetic Regenerative Refrigerators", in *Advances in Cryogenic Engineering*, vol. 41, pp. 1653, 1996.

[18] Dikeos, J., "Development and Validation of an Active Magnetic Regenerator Cycle Simulation*", MaSc Thesis*, University of Victoria, Victoria 2006.

[19] Wikipedia oline Encyclopedia, http://en.wikipedia.org/wiki/Regenerative_heat_exchanger.

[20] J.A. Barclay, Active and passive magnetic regenerators in gas/magnetic refrigerators*, Journal of Alloys and Compounds*, 207/208 (1994) 355-361.

[21] F.W Schmidt, A.J. Wilmott, Thermal energy storage and regeneration*, Hemisphere* Washington DC, 1981.

[22] W.M. Kays, A.L. London , Compact Heat Exchangers, Krieger Pub. Co., 3rd Sub-Eddition 2003.

[23] R.K. Shah, D.P. Sekulic, Fundamentals of Heat Exchanger Design, John Wiley & Sons, 2003.

[24] N. Wakao, S. Kaguei, Heat and Mass Transfer in Packed beds, Gordon and Breach Science Publishers, 1982.

[25] E. Achenbach, Heat and Flow Characteristics of Packed beds, *Experimental Thermal and Fluid Science* Vol.10-Nr.1, 1995.

[26] C.T. Hsu, Dynamic modeling of convective heat transfer in porous media, *Handbook of porous media*, CRC Press 2005.

[27] C. Hinchcliffe, A.J. Willmott, Lumped Heat-Transfer Coefficients for Thermal Regenerators, *International Journal of Heat andMass Transfer*, Vol.24No.7, 1981.

[28] H. K. Engelbrecht, A Numerical Model of an Active Magnetic Refrigerator with Experimental Validation, PhD Report University of Wisconsin, Madison, 2008.

[29] Macias-Machin, A. Oufer, L. N. WannemacherR, Heat Transfer between an Immersed Wire and a Liquid Fluidized Bed, Powder Technology 66:281-284, 1991.

[30] G.T. Lee, B.H. Kang, J.H. Lee, Effectiveness Enhancement of a Thermal Regenerator in Oscillating Flow, Applied Thermal Engineering Vol. 18 No.8, 1997.

[31] D.E. Daney, Regenerator Performance with Sinusoidal Flow, Cryogenics, Vol. 3, 1991.

[32] Y. Chen, E. Luo, W. Dai, Heat Transfer Characteristics of Oscillating Flow Regenerator Filled with Circular Tubes or Parallel Plates, Cryogenics, Vol. 47, 2007.

[33] T.W. Simon, J.R.Seume, A Survey of Oscillating Flow in Stirling Heat Exchangers, NASA Contractor Report 182108, 1988.

[34] T. Zhao, P. Cheng, Oscillatory Heat Transfer in a Pipe Subjected to a Laminar Reciprocating Flow, ASME Journal of Heat Transfer, Vol. 118, 1996.

[35] Swift G.W., Ward W.C., 1996, Simple harmonic analysis of regenerators, Journal of Thermophysics and Heat Transfer, 10(4):652-662.

[36] M. Kaviany, Principles of Heat Transfer in Porous Media, Springer 1995.

[37] Mahmoud M., Ghassemlooy Z. A. 2003, Tunable Fiber Bragg Gratings Modeling and Simulation, Proceedings of the 36th Annual Simulation Symposium (ANSS'03)

[38] Incropera, Frank P.; DeWitt, David P. (2007). Fundamentals of Heat and Mass Transfer (6th ed.). Hoboken: Wiley. pp. 519.

[39] M. M. Yovanovich, and Y.S. Muzychka, Modeling Nusselt Numbers for Thermally Developing Laminar Flow in Non-Circular Ducts, 7th AIAA/ASME Joint Thermophysics and Heat Transfer Conference, 1998.